*J. Fluid Mech.* (2024), *vol*. 985, A34, doi:10.1017/jfm.2024.319

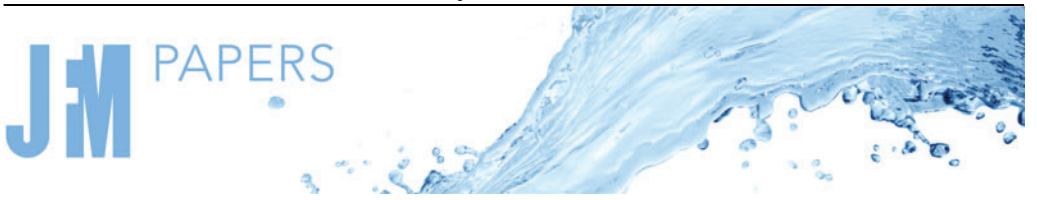


# Lagrangian dynamics and regularity of the spin Euler equation

**Zhaoyuan Meng**[1] **and Yue Yang**[1,2],†

[1]State Key Laboratory for Turbulence and Complex Systems, College of Engineering, Peking University, Beijing 100871, PR China

[2]HEDPS-CAPT, Peking University, Beijing 100871, PR China

(Received 30 October 2023; revised 25 March 2024; accepted 27 March 2024)

We derive the spin Euler equation for ideal flows by applying the spherical Clebsch mapping. This equation is based on the spin vector, a unit vector field encoding vortex lines, instead of the velocity. The spin Euler equation enables a feasible Lagrangian study of fluid dynamics, as the isosurface of a spin-vector component is a vortex surface and material surface in ideal flows. We establish a non-blowup criterion for the spin Euler equation, suggesting that the Laplacian of the spin vector must diverge if the solution forms a singularity at some finite time. The direct numerical simulations (DNS) of three ideal flows – the vortex knot, the vortex link and the modified Taylor–Green flow – are conducted by solving the spin Euler equation. The evolution of the Lagrangian vortex surface illustrates that the regions with large vorticity are rapidly stretched into spiral sheets. The DNS result exhibits a pronounced double-exponential growth of the maximum norm of Laplacian of the spin vector, showing no evidence of the finite-time singularity formation if the double-exponential growth holds at later times. Moreover, the present criterion with Lagrangian nature appears to be more sensitive than the Beale–Kato–Majda criterion in detecting the flows that are incapable of producing finite-time singularities.

**Key words:** topological fluid dynamics, vortex dynamics

## 1. Introduction

The dynamics of an ideal flow is governed by the three-dimensional (3-D) incompressible Euler equation. We apply the spherical Clebsch mapping (Kuznetsov & Mikhailov 1980) to develop the spin Euler equation based on the spin vector – a unit vector encoding vortex lines – instead of the velocity. Given a smooth initial spin vector with proper boundary conditions, the spin Euler equation is equivalent to the classical Euler equation. The spin Euler equation facilitates a viable Lagrangian study of fluid dynamics, as the isosurface

† Email address for correspondence: yyg@pku.edu.cn

of a spin-vector component is a vortex surface (Yang & Pullin 2010; Yang, Xiong & Lu 2023). On the other hand, a globally smooth spin vector may not exist for a given velocity field with vorticity nulls or unclosed vortex lines. Hence the spin Euler equation admits only a subset of initial conditions of the Euler equation.

The present study employs the spin Euler equation to examine the possibility of a finite-time singularity in ideal flows. One of the outstanding open problems in fluid mechanics is whether smooth initial data can lead to finite-time singularities in the ideal flow. This problem is closely related to the existence and smoothness of solutions to the Navier–Stokes equation (e.g. Fefferman 2001; Doering 2009; Wei 2016; Ayala & Protas 2017).

The regularity of the incompressible Euler equation has been studied extensively. Various criteria for blowup and non-blowup, based on different quantities and techniques, have been reviewed by Chae (2008), Gibbon (2008) and Drivas & Elgindi (2023). Several criteria relate the occurrence of singularity to the growth of the vorticity $\boldsymbol{\omega}$, which plays a vital role in fluid dynamics. The Beale–Kato–Majda (BKM) criterion establishes a sufficient condition for the regularity in terms of $\boldsymbol{\omega}$ (Beale, Kato & Majda 1984). The geometric criterion of Constantin, Fefferman & Majda (1996) relates the regularity of the velocity to the smoothness of the vorticity direction. Moreover, there are some refined analytical criteria for blowup (e.g. Planchon 2003; Zhou & Lei 2013).

The regularity of the incompressible Euler equations has also been investigated by large-scale numerical simulations. Brachet *et al.* (1983, 1992) and Bustamante & Brachet (2012) conducted numerical studies of the evolution of the inviscid Taylor–Green flow, and showed a near-exponential growth of the maximum vorticity over time, with regions of the high vorticity predominantly confined within thin, sheet-like structures. The formation of vortex sheets reduces the three-dimensionality, which suppresses the formation of a finite-time singularity (Constantin *et al.* 1996; Drivas & Elgindi 2023).

As the regularity of the two-dimensional (2-D) Euler equations was established (Yudovich 1963; Majda & Bertozzi 2002), subsequent numerical studies focused primarily on the carefully designed initial condition that would enhance the vorticity growth. However, different vorticity growth trends were observed in the numerical simulations with different initial conditions or even the same initial condition.

For the two perturbed anti-parallel vortex tubes, Kerr (1993, 2005) found $\|\boldsymbol{\omega}\|_\infty \sim (t_0 - t)^{-1}$, which provided strong evidence in favour of blowup, whereas Hou & Li (2007) and Hou (2009) obtained a high-resolution numerical solution that is still regular beyond the presumed blowup time $t_0$, and exhibited a maximum vorticity growth slower than double-exponential. The analysis was subsequently revisited in Bustamante & Kerr (2008), who proposed a hypothesis of vorticity growth $\|\boldsymbol{\omega}\|_\infty \sim (t_0 - t)^{-\gamma}$, with $\gamma > 1$, and in Kerr (2013), who reported a double-exponential growth.

The vorticity growth of $\|\boldsymbol{\omega}\|_\infty \sim (t_0 - t)^{-1}$ was also observed in Grauer, Marliani & Germaschewski (1998) using a perturbed cylindrical shear flow, and in Orlandi, Pirozzoli & Carnevale (2012) using the collision of two Lamb dipoles. Agafontsev, Kuznetsov & Mailybaev (2015, 2017) reported that the vorticity grows exponentially in time in a shear flow with random perturbations. Moreover, Ricca, Samuels & Barenghi (1999) suggested that the vortex knot is a useful configuration for studying singularity formation, and also pointed out the lack of study on the evolution of vortex knots or links with finite thickness in ideal flows.

Several studies examined the Kida–Pelz flow (Kida 1985; Boratav & Pelz 1994; Pelz 2001), which is another highly symmetric flow for investigating the formation of potential finite-time singularity. Grafke *et al.* (2008) compared different numerical methods applied

to a Kida–Pelz flow in spectral and real spaces, and found no evidence of blowup at the times predicted by previous studies, which was confirmed by Hou & Li (2008). They also observed that the vorticity increases exponentially along the Lagrangian trajectory.

Furthermore, there are several studies that are not based on the Euler equation for investigating potential finite-time singularities in ideal flows. Campolina & Mailybaev (2018) developed a model identical to the Euler equations by imitating the calculus on a 3-D logarithmic lattice. This model for ideal flows elucidates the emergence of singularities as a manifestation of a chaotic attractor in a renormalized dynamical system. Their results implied that the direct numerical simulations (DNS) with the available resolution are inadequate for the analysis of singularity formation for the Euler equation. By employing a level-set representation for the vorticity field, Constantin (2001*a*,*b*) and Deng, Hou & Yu (2005) established global existence theorems for a wide range of initial values, and revealed the geometric structures of plausible blowup scenarios, for the 3-D Euler equations and the 3-D Lagrangian averaged Euler equations.

In the present study, we investigate the Lagrangian dynamics and regularity of the spin Euler equation, and derive a new non-blowup condition for ideal flows. The DNS were conducted for solving the spin Euler equation with the pseudo-spectral method in various inviscid vortical flows. The outline of the present paper is as follows. Section 2 introduces the spin Euler equation and derives the non-blowup condition. Section 3 describes numerical set-ups and methods. Section 4 elucidates Lagrangian dynamics of ideal flows and assesses the non-blowup criterion. Some conclusions are drawn in § 5.

## 2. Theoretical framework of the spin Euler equation

### 2.1. *Introduction to the spin Euler equation*

The 3-D incompressible Euler equation is

$$\partial_t \boldsymbol{u} + \boldsymbol{u} \cdot \boldsymbol{\nabla} \boldsymbol{u} = -\boldsymbol{\nabla} p, \tag{2.1}$$

with $\boldsymbol{\nabla} \cdot \boldsymbol{u} = 0$, where $\boldsymbol{u}$ is the velocity, and $p$ is the pressure.

By applying the spherical Clebsch mapping with a Hamiltonian structure (Kuznetsov & Mikhailov 1980), (2.1) is transformed into a Lagrangian form

$$\partial_t \boldsymbol{s} + \boldsymbol{u} \cdot \boldsymbol{\nabla} \boldsymbol{s} = \boldsymbol{0}, \tag{2.2}$$

where $\boldsymbol{s}$ is of class $C^k$, $k \geq 1$. Note that $\boldsymbol{u}$ can be obtained from $\boldsymbol{s}$, which is discussed further in (3.1). Here, the Hopf fibration (Hopf 1931)

$$\boldsymbol{s} = (a^2 + b^2 - c^2 - d^2, 2(bc - ad), 2(ac + bd)) \tag{2.3}$$

with $|\boldsymbol{s}| = 1$ establishes a correspondence between the unit spin vector $\boldsymbol{s} \in \mathbb{S}^2$ and a two-component wave function $\boldsymbol{\psi} = [\psi_1, \psi_2]^{\mathrm{T}} \in \mathbb{S}^3$ (Chern *et al.* 2016; Chern 2017), where $\psi_1 = a + \mathrm{i}b$ and $\psi_2 = c + \mathrm{i}d$ are complex functions of real-valued potentials $a, b, c, d$, and i denotes the imaginary unit. The Clebsch potentials $a, b, c, d$ are subject to the constraint $a\,\Delta b - b\,\Delta a + c\,\Delta d - d\,\Delta c = 0$, which ensures the incompressibility $\boldsymbol{\nabla} \cdot \boldsymbol{u} = 0$.

Then the velocity and vorticity $\boldsymbol{\omega} \equiv \nabla \times \boldsymbol{u}$ can be re-expressed by $\boldsymbol{u} = a\nabla b - b\nabla a + c\nabla d - d\nabla c$ and

$$\begin{aligned}\boldsymbol{\omega} &= \tfrac{1}{4}\varepsilon_{ijk} s_i \nabla s_j \times \nabla s_k \\ &= \tfrac{1}{2}\left(s_1 \nabla s_2 \times \nabla s_3 + s_2 \nabla s_3 \times \nabla s_1 + s_3 \nabla s_1 \times \nabla s_2\right),\end{aligned} \tag{2.4}$$

respectively, where $\varepsilon_{ijk}$ is the Levi–Civita symbol. The derivation of (2.4) is detailed in Appendix A. Note that $\boldsymbol{s}$ remains a gauge invariant in the transformation from the velocity to 'magnetization' (Chorin 1994).

From the perspective of vortex dynamics, the spin vector encodes vortex lines and surfaces (Chern *et al.* 2016; Chern 2017; Yang *et al.* 2023). Isosurfaces of one component of $\boldsymbol{s}$ are a family of vortex surfaces. Correspondingly, intersections of isosurfaces of two components of $\boldsymbol{s}$ are a family of vortex lines.

We consider the quaternion form (Gibbon & Holm 2007) of the two-component wave function $\boldsymbol{\psi} = a + \boldsymbol{i}b + \boldsymbol{j}c + \boldsymbol{k}d$, where $\{\boldsymbol{i}, \boldsymbol{j}, \boldsymbol{k}\}$ are the basis vectors of the imaginary part of the quaternion. The velocity and spin vector are then given by $\boldsymbol{u} = (\nabla\bar{\boldsymbol{\psi}}\boldsymbol{i}\boldsymbol{\psi} - \bar{\boldsymbol{\psi}}\boldsymbol{i}\nabla\boldsymbol{\psi})/2$ and $\boldsymbol{s} = \bar{\boldsymbol{\psi}}\boldsymbol{i}\boldsymbol{\psi}$, respectively, where $\bar{\boldsymbol{\psi}}$ denotes the quaternion conjugate of $\boldsymbol{\psi}$. Then we derive

$$\begin{aligned}\boldsymbol{u}\cdot\nabla\boldsymbol{s} &= \tfrac{1}{2}\left(\nabla\bar{\boldsymbol{\psi}}\boldsymbol{i}\boldsymbol{\psi}\cdot\nabla\bar{\boldsymbol{\psi}}\boldsymbol{i}\boldsymbol{\psi} - |\nabla\boldsymbol{\psi}|^2 + |\nabla\boldsymbol{\psi}|^2 - \bar{\boldsymbol{\psi}}\boldsymbol{i}\nabla\boldsymbol{\psi}\cdot\bar{\boldsymbol{\psi}}\boldsymbol{i}\nabla\boldsymbol{\psi}\right) \\ &= \tfrac{1}{2}\left(\boldsymbol{s}\nabla\bar{\boldsymbol{\psi}}\cdot\boldsymbol{i}\nabla\boldsymbol{\psi} - \nabla\bar{\boldsymbol{\psi}}\cdot\boldsymbol{i}\nabla\boldsymbol{\psi}\boldsymbol{s}\right) = \boldsymbol{s}\times\boldsymbol{m},\end{aligned} \tag{2.5}$$

where $\boldsymbol{m} \equiv \nabla\bar{\boldsymbol{\psi}}\cdot\boldsymbol{i}\nabla\boldsymbol{\psi}$ is a pure quaternion (i.e. a vector in $\mathbb{R}^3$) and can be expanded as $\boldsymbol{m} = \boldsymbol{i}m_1 + \boldsymbol{j}m_2 + \boldsymbol{k}m_3$, with

$$\left.\begin{aligned} m_1 &= |\nabla a|^2 + |\nabla b|^2 - |\nabla c|^2 - |\nabla d|^2, \\ m_2 &= 2(\nabla b\cdot\nabla c - \nabla a\cdot\nabla d), \\ m_3 &= 2(\nabla a\cdot\nabla c + \nabla b\cdot\nabla d). \end{aligned}\right\} \tag{2.6}$$

Thus we rewrite $\boldsymbol{u}\cdot\nabla\boldsymbol{s} = \boldsymbol{s}\times\boldsymbol{m}$ with an effective field $\boldsymbol{m} = (m_1, m_2, m_3)$.

In general, $\boldsymbol{m}$ cannot be represented solely in terms of $\boldsymbol{s}$, because the Hopf mapping (2.3) is non-invertible. However, given $\boldsymbol{s}$ with a boundary condition, we can obtain $\boldsymbol{u}$ by calculating $\boldsymbol{\omega}$ with (2.4) and applying the generalized Biot–Savart law, and then obtain $\boldsymbol{s}\times\boldsymbol{m}$ at any point in $\mathbb{R}^3$ by (2.5).

Substituting (2.5) into (2.2), we obtain the spin Euler equation

$$\partial_t\boldsymbol{s} + \boldsymbol{s}\times\boldsymbol{m} = \boldsymbol{0}. \tag{2.7}$$

This is equivalent to the original incompressible Euler equation (2.1). In contrast to (2.2), (2.7) characterizes the evolution of $\boldsymbol{s}$ by its precession about $\boldsymbol{m}$ rather than the convection with $\boldsymbol{u}$. The spin Euler equation (2.7) can be more suitable to study fluid dynamics from a Lagrangian perspective than its original form (2.1), because the isosurfaces of $s_i$, $i = 1, 2, 3$, are vortex surfaces consisting of vortex lines (Yang & Pullin 2010, 2011; Yang *et al.* 2023). From the Helmholtz vorticity laws, the surfaces are material surfaces for all $t \geq 0$ in Euler flows.

Therefore, solving the spin Euler equation (2.7) is similar to a vortex method (Yang *et al.* 2021; Nabizadeh *et al.* 2022; Xiong *et al.* 2022) for simulating ideal flows. Since the primary variable $\boldsymbol{s}$ of (2.7) has unit length, the fixed magnitude of $\boldsymbol{s}$ can avoid the numerical blowup arising from numerical instabilities.

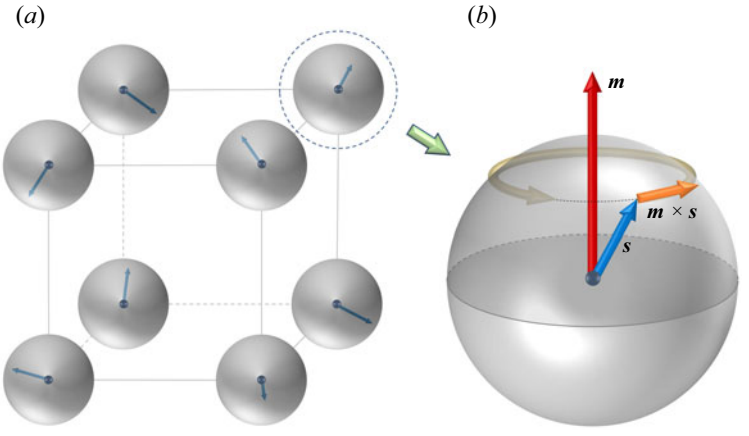


Figure 1. The domain is discretized on a uniform grid. The smallest lattice configuration, consisting of $2^3$ grid points, is sketched. (*a*) Schematic of a $2^3$ lattice of spin vectors, where the orientation of $\boldsymbol{s}$ fully characterizes the ideal flow by (2.4). (*b*) At each grid point, the spin vector $\boldsymbol{s}$ in (2.3) precesses around an 'effective magnetic field' $\boldsymbol{m}$ in (2.6).

In particular, the spin Euler equation contains the inherent Lagrangian vortex dynamics via level sets of $s_i$ (i.e. vortex surfaces). This can facilitate the regularity analysis of the Euler equation, similar to the level set representation of $\boldsymbol{\omega}$ (Constantin 2001*a*,*b*; Deng *et al.* 2005).

Note that the initial conditions $\boldsymbol{s}_0$ of (2.7) for simulating ideal flows are a subset of the classical Euler equations, because finding a globally smooth $\boldsymbol{s}_0$ for a given vorticity field $\boldsymbol{\omega}_0$ remains an open problem. Currently, a useful approximation of $\boldsymbol{s}_0$ can be obtained using the numerical optimization (Chern *et al.* 2017) and the Poincaré recurrence theorem (Poincaré 1890).

The spin Euler equation is also equivalent to a special case of the Landau–Lifshitz equation with a specific effective magnetic field $\boldsymbol{m}$, revealing a possible connection between ideal flow and magnetic crystal. As sketched in figure 1, the spin vector (or magnetization) $\boldsymbol{s}$ in (2.3) at each point in space precesses around the effective magnetic field $\boldsymbol{m}$ in (2.6). More discussion is provided in Appendix B.

### 2.2. *Non-blowup condition of the spin Euler equation*

Next, we discuss the regularity of the spin Euler equation. The derivation for the non-blowup condition is outlined below and detailed in Appendix C. First, we estimate the upper bound of $\|\boldsymbol{\omega}\|_p$ in terms of $\|\nabla \boldsymbol{s}\|_{2p}$, $p \geq 1$, as

$$\|\boldsymbol{\omega}\|_p \leq \tfrac{1}{2} \|\nabla \boldsymbol{s}\|_{2p}^2, \tag{2.8}$$

where the $L^p$-norm is defined in Appendix C. Then we estimate the growth of $\|\nabla \boldsymbol{s}\|_{2p}$ as

$$\partial_t \|\nabla \boldsymbol{s}\|_{2p}^{2p} \leq 2p \, \|\boldsymbol{m}\|_1 \, \|\Delta \boldsymbol{s}\|_\infty^p, \tag{2.9}$$

and the upper bound of $\|\boldsymbol{m}\|_1$ in terms of $\|\nabla \boldsymbol{s}\|_2$ and $\|\Delta \boldsymbol{s}\|_\infty$ as

$$\|\boldsymbol{m}\|_1 \leq \tfrac{1}{4} \|\nabla \boldsymbol{s}\|_2^2 \left(\sqrt{6} + \sqrt{2} C_\omega \, \|\Delta \boldsymbol{s}\|_\infty\right), \tag{2.10}$$

where $C_\omega$ is a positive constant. Finally, substituting (2.9) and (2.10) into (2.8), we obtain a sufficient condition for bounded $\|\boldsymbol{\omega}\|_p$ as

$$\int_0^t \|\Delta \boldsymbol{s}(\cdot, \tau)\|_\infty^{p+1} \,\mathrm{d}\tau < \infty, \quad \forall p \geq 1. \tag{2.11}$$

In summary, we obtain a non-blowup condition (2.11) of the spin Euler equation (equivalent to the original Euler equation with well-posed initial conditions), which guarantees a bounded $\|\boldsymbol{\omega}\|_p$. It implies that if the solution loses regularity beyond a certain time, then the Laplacian of the spin vector must grow unboundedly. The transport equation and the estimation of the norm of $\Delta \boldsymbol{s}$ are discussed further in Appendix D.

## 3. Numerical set-up

We conduct the DNS of three ideal flows with different initial conditions in a periodic cube of side $2\pi$ on $N^3$ (up to $1536^3$) uniform grid points, by solving the spin Euler equation (2.2) with the pseudo-spectral method as

$$\left.\begin{aligned} &\frac{\partial \boldsymbol{s}}{\partial t} = \mathcal{F}^{-1}\left[\frac{1}{|\boldsymbol{\kappa}|^2}\,\mathrm{i}\mathcal{F}\left(\frac{1}{4}\,\varepsilon_{ijk} s_i\, \boldsymbol{\nabla} s_j \times \boldsymbol{\nabla} s_k\right) \times \boldsymbol{\kappa}\right] \cdot \boldsymbol{\nabla} \boldsymbol{s}, \\ &\boldsymbol{s}(\boldsymbol{x}, t=0) = \boldsymbol{s}_0(\boldsymbol{x}). \end{aligned}\right\} \tag{3.1}$$

Here, $\boldsymbol{u}$ is calculated from $\boldsymbol{\omega}$ with (2.4) by the Biot–Savart law in Fourier space (Xiong & Yang 2020), $\boldsymbol{\kappa}$ denotes the wavenumber vector, $\boldsymbol{s}_0$ is a smooth initial condition, and $\mathcal{F}$ is the Fourier transform operator with its inverse form $\mathcal{F}^{-1}$. The high-order Fourier smoothing method (Hou & Li 2007; Bustamante & Kerr 2008) is used to suppress the Gibbs phenomenon. The temporal evolution is integrated using an explicit second-order Runge–Kutta scheme with adaptive time steps in physical space. The time step is selected to ensure that the Courant–Friedrichs–Lewy number is smaller than 0.3 for numerical stability and accuracy. In the numerical implementation, $\boldsymbol{s}$ is normalized at every time step to ensure $|\boldsymbol{s}| = 1$.

We consider two types of initial conditions. For the first type, the initial vorticity is concentrated in a thin closed vortex tube, such as the trefoil knot (Yao, Yang & Hussain 2021; Zhao & Scalo 2021; Zhao *et al.* 2021) and Hopf link (Aref & Zawadzki 1991; Kivotides & Leonard 2021; Yao *et al.* 2022). Under the self-induced velocity, such vortex tubes can be gradually stretched, twisted and flattened, and form nearly singular vortical structures.

We use the rational map (Kedia *et al.* 2016; Tao *et al.* 2021) to construct smooth $\boldsymbol{s}_0$. A small twist is applied to the vortex tube by setting $P = \alpha$ (Tao *et al.* 2021), and $Q = \alpha^3 + \beta^2$ and $Q = \alpha^2 + \beta^2$ are chosen for the trefoil knot and the Hopf link, respectively. Here, $(P, Q)$ are a pair of complex polynomial functions, and $(\alpha, \beta)$ is a mapping of the coordinate system from the Euclidean space $\mathbb{R}^3$ to the two-component complex space $\mathbb{C}^2$. The function pair $(P, Q)$ is normalized and subjected to a divergence-free projection, yielding a two-component wave function $\boldsymbol{\psi}_0 = [\psi_{1,0}, \psi_{2,0}]^{\mathrm{T}}$ that matches the initial field. The initial spin vector $\boldsymbol{s}_0$ and vorticity $\boldsymbol{\omega}_0$ are then obtained from (2.3) and (2.4), respectively. Additionally, we re-scale the time as $t^* = t/(L_0^2/\Gamma)$, with the initial mean length $L_0 = 2\sqrt{2}\pi^{3/2}/\|\boldsymbol{\nabla} \boldsymbol{s}(\cdot, 0)\|_2$ and the circulation $\Gamma$. The trefoil knot has $L_0 = 0.749$ and $\Gamma = 5.05$, and the Hopf link has $L_0 = 0.773$ and $\Gamma = 5.24$.

| Cases | $N^3$ | $\|\boldsymbol{u}_0\|_2^2$ | $\mathcal{H}_0$ | $L_0$ | $\Gamma$ | $t^*/t$ | $T_\mathcal{R}$ |
|---|---|---|---|---|---|---|---|
| Trefoil knot | Up to $1536^3$ | 72.4 | 79.0 | 0.749 | 5.05 | 9.00 | 2.39 |
| Hopf link | Up to $1536^3$ | 68.9 | 79.0 | 0.773 | 5.24 | 8.77 | 2.61 |
| MTG | Up to $1024^3$ | 20.7 | 0 | — | — | 1 | 3.67 |

Table 1. DNS cases and parameters.

The second type is a modified Taylor–Green (MTG) initial condition (Meng & Yang 2023), with

$$\boldsymbol{s}_0 = (\cos x \cos y \cos z, \sqrt{1 - \cos^2 x \cos^2 y \cos^2 z}\, \cos 2z, \sqrt{1 - \cos^2 x \cos^2 y \cos^2 z}\, \sin 2z) \tag{3.2}$$

and

$$\boldsymbol{\omega}_0 = (\cos x \sin y \cos z, -\sin x \cos y \cos z, 0). \tag{3.3}$$

Note that $\boldsymbol{s}_0$ for this MTG initial condition is different from $\boldsymbol{s}_0$ for the standard Taylor–Green initial condition (Taylor & Green 1937; Brachet *et al.* 1983, 1992; Bustamante & Brachet 2012); the former in (3.2) has a negligible singularity, and the latter has a weak singularity (Meng & Yang 2023). This highly symmetric MTG flow would not exhibit a finite-time singularity, and this non-blowup case is used to validate the criterion in (2.11). The re-scaling time is $t^* = t$. The parameters for all cases are listed in table 1.

To evaluate the numerical resolution, we define $\mathcal{R}(t^*) \equiv 1/(h\,\|\nabla \boldsymbol{s}(\cdot, t^*)\|_\infty)$, the ratio of the minimum resolved scale to the grid spacing $h$. A finer resolution has a larger $\mathcal{R}$. The evolution of $\mathcal{R}$ for the three initial conditions is shown in figures 2(*a*)–2(*c*). Our numerical tests suggest that $\mathcal{R} \geq 2$ can be the criterion for well resolving the smallest scale of (3.1). The largest numbers of grid points in the simulation are $N^3 = 1536^3$ for the trefoil knot and the Hopf link, and $N^3 = 1024^3$ for the MTG flow. Based on the criterion, the largest time $T_\mathcal{R} \equiv t^*|_{\mathcal{R}=2}$ of the simulation with the satisfactory resolution is given in table 1 for each case.

Additionally, the resolution can be assessed by the conservation of the total energy $\|\boldsymbol{u}\|_2^2$ and the helicity $\mathcal{H} = \int_\mathcal{D} \boldsymbol{u} \cdot \boldsymbol{\omega}\, \mathrm{d}V$ (Moreau 1961; Moffatt 1969; Meng, Shen & Yang 2023), which are two invariants of the Euler equations. The energy loss is less than 1‰ for $\mathcal{R} \geq 2$ in figures 2(*d*)–2(*f*), and the helicity is also well conserved in figures 2(*g*)–2(*i*).

## 4. Validation of non-blowup conditions for the spin Euler equation

### 4.1. *Evolution of vortex surfaces*

The DNS of the spin Euler equation (2.7) are carried out to investigate Lagrangian dynamics of ideal flows listed in table 1, and to validate the non-blowup criterion (2.11). To illustrate the Lagrangian vortex dynamics, figure 3 shows the top view of the isosurface of $s_1 = 0.5$ (i.e. vortex surface) for the trefoil knot at $t^* = 0$, 0.9 and 1.8. Note that isosurfaces of $s_2$ and $s_3$ can show similar structures (Tao *et al.* 2021), and the isosurfaces of $|\boldsymbol{\omega}|$ (not shown) fail to capture the complete vortex tube as visualized by $s_1$ (as discussed in Xiong & Yang 2019; Shen *et al.* 2023).

Near the three crossings of the initial vortex knot, adjacent parts of the vortex tube are nearly orthogonal. Driven by the self-induced velocity with the Biot–Savart law, the vortex tube and vortex lines are stretched and twisted. The adjacent parts of the vortex

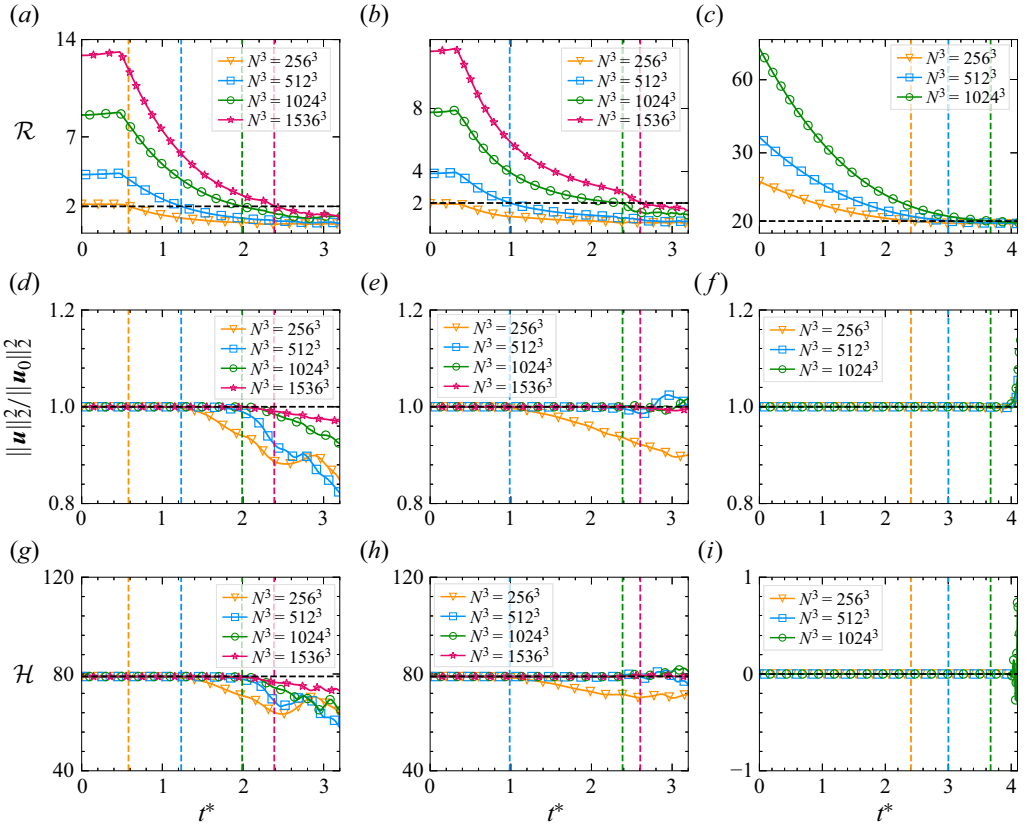


Figure 2. Evolution of (*a–c*) $\mathcal{R}(t^*) \equiv 1/(h\,\|\nabla \boldsymbol{s}(\cdot, t^*)\|_\infty)$, (*d–f*) $\|\boldsymbol{u}\|_2^2/\|\boldsymbol{u}_0\|_2^2$ and (*g–i*) the helicity, for the (*a*,*d*,*g*) trefoil knot, (*b*,*e*,*h*) Hopf link and (*c*,*f*,*i*) MTG flow, with different grid resolutions. The vertical dashed lines with different colours mark the time with $\mathcal{R} = 2$ for each resolution. The simulations are well-resolved on the left of the dashed lines.

knot approach each other, and they are progressively flattened and rolled up, instead of undergoing the vortex reconnection in viscous flows (Yao & Hussain 2022). The regions with large vorticity magnitude $|\boldsymbol{\omega}|$ are rapidly stretched into spiral sheets with strong twist.

In figure 3, the evolving vortex surfaces and lines preserve their initial mapping to the red circle and cyan points on $\mathbb{S}^2$, respectively, due to the Lagrangian nature of the spin Euler equation. Namely, the vortex topology is preserved in ideal flows. In addition, figure 4 shows the top view of the isosurface of $s_1 = 0.5$ for the Hopf link at $t^* = 0$, 0.88 and 2.19. The structural evolution is similar to that of the trefoil knot.

Figure 5 plots the contour of $|\boldsymbol{\omega}|$ on the $x$–$y$ plane at $z = 2.55$, and on the $y$–$z$ plane at $x = 3.24$ for the trefoil knot, along with the contour lines of $s_1$. These planes intersect the point with the largest $|\boldsymbol{\omega}|$, so their contours show the most intense swirling motion. In figure 5(*b*), 'vorticity pancakes' (Brachet *et al.* 1992) form in the regions of large $|\boldsymbol{\omega}|$ among highly stretched and curved vortex surfaces. These structures appear when the vortex surfaces approach each other and undergo strong deformation. The formation of the high-vorticity region within sheet-like structures was observed in the collapse of vortex pairs (e.g. Pumir & Siggia 1990; Kerr 1993) and Taylor–Green and Kida–Pelz flows (Yang & Pullin 2010). Furthermore, we observe the energy spectra with the $k^{-3}$ scaling (not

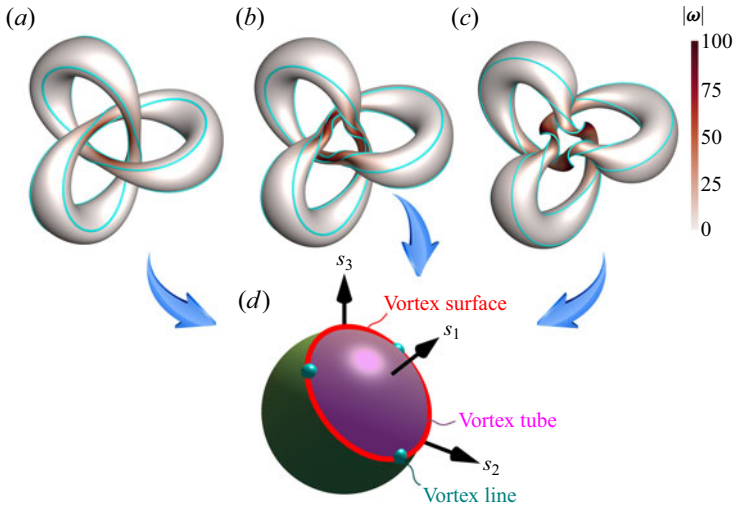


Figure 3. (*a–c*) Evolution of the isosurface of $s_1 = 0.5$ (vortex surfaces) colour-coded by $|\boldsymbol{\omega}|$ for the trefoil knot at $t^* = 0, 0.9$ and 1.8 in the top view. Some vortex lines (cyan) are integrated and plotted on the isosurfaces. (*d*) The vortex surface for $s_1 = 0.5$, the region enclosed by this vortex surface, and the three cyan vortex lines are mapped to the red circle, the purple spherical cap within the red circle, and the three cyan points on the Bloch sphere $\mathbb{S}^2$, respectively.

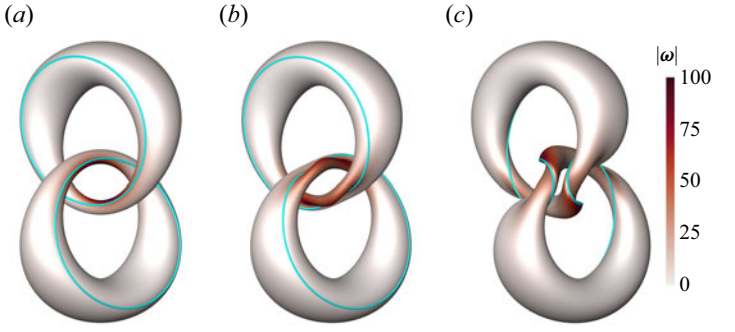


Figure 4. Evolution of the isosurface of $s_1 = 0.5$ (vortex surface) colour-coded by $|\boldsymbol{\omega}|$ for the Hopf link at $t^* = 0, 0.88$ and 2.19 in the top view. Some vortex lines (cyan) are integrated and plotted on the isosurfaces.

shown) in the evolution of the trefoil knot and Hopf link, consistent with the result for the collision of two Lamb dipoles in Orlandi *et al.* (2012).

In the highly symmetric MTG flow, a finite-time singularity may not occur according to the theoretical analysis (Constantin *et al.* 1996). Figure 6 plots the evolution of the isosurfaces of $s_1 = 0.8$ (red) and $s_1 = -0.8$ (blue) for the MTG flow. A pair of vortex blobs are compressed and flattened into pancakes. Since the vortex surface is compressed in a quasi-2-D configuration, preserving the smoothness $\nabla(\boldsymbol{\omega}/|\boldsymbol{\omega}|)$ of the vorticity direction (Constantin *et al.* 1996), the MTG flow does not exhibit a finite-time singularity, even though the vorticity grows rapidly (Brachet *et al.* 1992).

The comparison of the two types of ideal flows implies that the Euler equation cannot form a singularity in a 2-D process. Constantin *et al.* (1996) proved that if $\boldsymbol{u}$ remains uniformly bounded and $\boldsymbol{\omega}/|\boldsymbol{\omega}|$ stays $C^1$, then no singularity can occur. In other words, the vorticity must change its direction very rapidly to form a potential singularity. Note that if

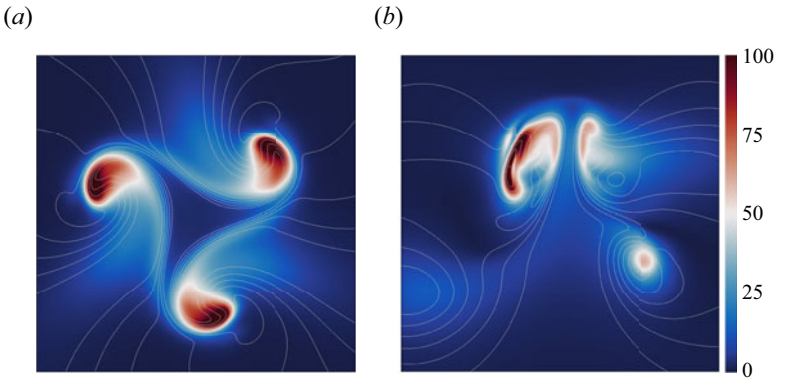


Figure 5. Contour of the vorticity magnitude and contour lines (white) of $s_1$ for the trefoil knot on (*a*) the $x$–$y$ plane at $z = 2.55$, and (*b*) the $y$–$z$ plane at $x = 3.24$, at $t^* = 1.8$. The planes intersecting the point with the largest $|\boldsymbol{\omega}|$ contain the most intense swirling motion in the flow.

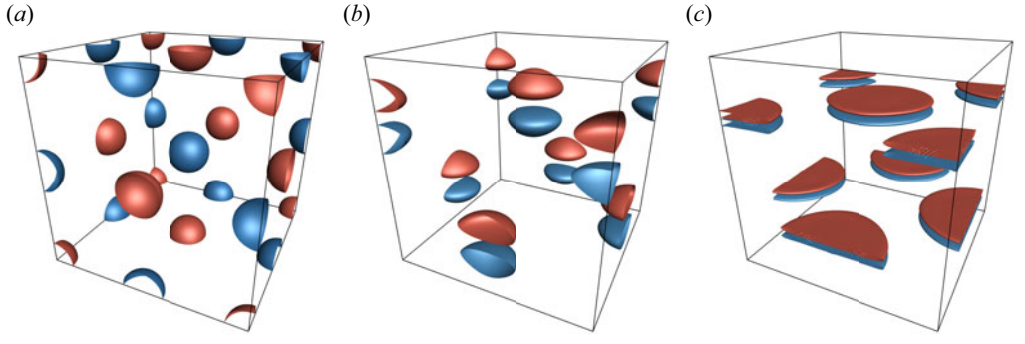


Figure 6. Evolution of the isosurfaces of $s_1 = 0.8$ (red) and $s_1 = -0.8$ (blue) in the MTG flow: (*a*) $t^* = 0$, (*b*) $t^* = 2$, (*c*) $t^* = 4$.

a singularity occurs at a vorticity null for all $t^* < t_b^*$ (e.g. Elgindi 2021), then the vorticity direction becomes discontinuous at the time of singularity. The MTG flow vortex lines near the vorticity nulls maintain a quasi-2-D smooth shape, which contradicts the necessary blowup conditions. Hence the MTG flow does not exhibit finite-time singularities. By contrast, the trefoil knot and Hopf link have large vortex-line curvature in figures 3(*c*) and 4(*c*), with a rapid change in the vorticity direction.

### 4.2. *Assessment of the non-blowup criterion*

We apply (2.11) to the three ideal flows to test the non-blowup criterion based on the spin Euler equation, and compare our criterion to the BKM criterion (Beale *et al.* 1984) by examining growth rates of the maximum vorticity and Laplacian spin vector. Before $t^* = T_{\mathcal{R}}$, $\|\boldsymbol{\omega}\|_\infty$ increases by a factor of approximately 16 for the trefoil knot and the Hopf link in figure 7. Both $\|\boldsymbol{\omega}\|_\infty$ and $\|\Delta \boldsymbol{s}\|_\infty$ exhibit the nearly double-exponential growth for the trefoil knot and Hopf link. The double-exponential growth of $\|\boldsymbol{\omega}\|_\infty$ is consistent with the results in Hou & Li (2007) and Kerr (2013). As the number of grid points increases (up to $1536^3$), the growth rate of $\|\Delta \boldsymbol{s}\|_\infty$ appears to remain constant for the trefoil knot and Hopf link.

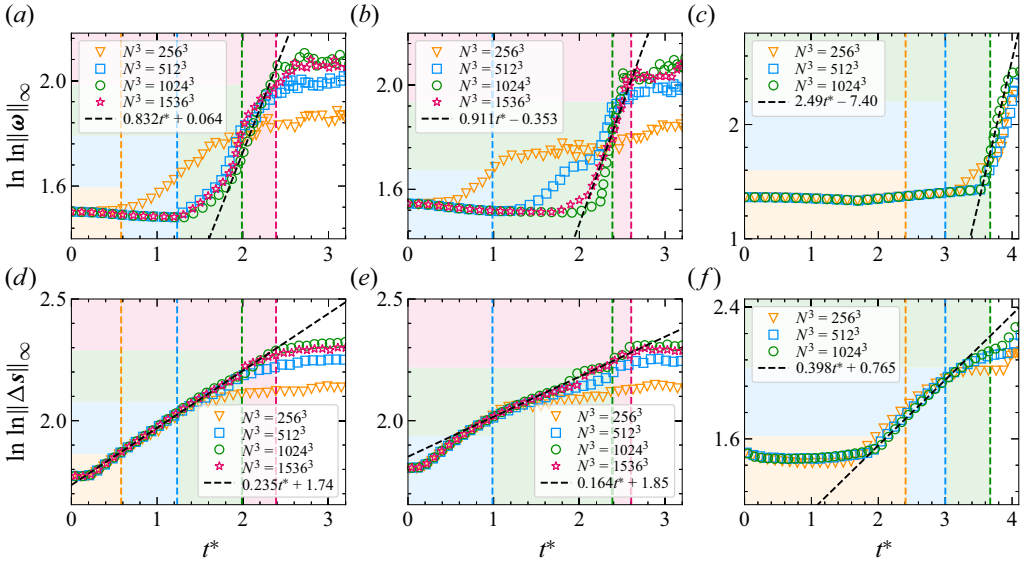


Figure 7. Evolution of (*a–c*) the maximum vorticity and (*d–f*) the maximum Laplacian spin vector, for (*a*,*d*) the trefoil knot, (*b*,*e*) the Hopf link and (*c*,*f*) MTG flow, with different grid resolutions, respectively. Note that we plot $\ln\ln(50\|\boldsymbol{\omega}\|_\infty)$ for the MTG flow, where the factor 50 is used to avoid complex values of the logarithm. The vertical dashed lines with different colours mark the time with $\mathcal{R} = 2$ for each resolution. The simulations are well-resolved on the left of the dashed lines (shaded in corresponding colours).

The present criterion has some advantages that $\ln\ln\|\Delta\boldsymbol{s}\|_\infty$ grows more slowly than $\ln\ln\|\boldsymbol{\omega}\|_\infty$ (4–6 times slower), and exhibits better convergence with the mesh resolution. Therefore, $\Delta\boldsymbol{s}$ appears to be resolved more easily than $\boldsymbol{\omega}$ with the same numerical accuracy. Moreover, the duration of the linear stage for $\ln\ln\|\Delta\boldsymbol{s}\|_\infty$ exceeds that for $\ln\ln\|\boldsymbol{\omega}\|_\infty$ more than five-fold.

The highly symmetric MTG flow shows no evidence of a finite-time singularity. The profile of $\ln\ln\|\Delta\boldsymbol{s}\|_\infty$ in figure 7(*f*) clearly bends downwards before $t^* = T_\mathcal{R}$ with $N^3 = 1024^3$. The growth rate of $\|\Delta\boldsymbol{s}\|_\infty$ is weaker than double-exponential, whereas the growth of $\|\boldsymbol{\omega}\|_\infty$ remains double-exponential in figure 7(*c*) when $t^* < T_\mathcal{R}$. Therefore, the criterion based on $\Delta\boldsymbol{s}$ can effectively identify the flows that are unlikely to develop a finite-time singularity.

Assuming that the double-exponential growth is bounded in a finite time $t$, the time integral of $\|\Delta\boldsymbol{s}\|_\infty^{p+1}$ becomes

$$\int_0^t \|\Delta\boldsymbol{s}(\cdot,\tau)\|_\infty^{p+1}\,\mathrm{d}\tau \le \frac{(\mathrm{e}^{c_1 t}-1)\exp[(p+1)\,\mathrm{e}^{c_1 t+c_2}]}{c_1\mathrm{e}^{c_1 t}}, \tag{4.1}$$

with constants $c_1$ and $c_2$. According to the non-blowup condition (2.11), the Euler equation can avoid singularity formation in finite time for the double-exponential growth of $\|\Delta\boldsymbol{s}\|_\infty$.

### 4.3. *Difference of non-blowup criteria*

We highlight the major difference between (2.11) and the BKM criterion, and explain why $\|\Delta\boldsymbol{s}\|_\infty$ grows more slowly than $\|\boldsymbol{\omega}\|_\infty$. Figure 8 plots the trajectories of $\arg\max|\boldsymbol{\omega}|$ and $\arg\max|\Delta\boldsymbol{s}|$, colour-coded by $t^*$, and their projections on the $x$–$y$ plane for the trefoil knot and Hopf link. The trajectories of $\arg\max|\boldsymbol{\omega}|$ and $\arg\max|\Delta\boldsymbol{s}|$ starting from the same

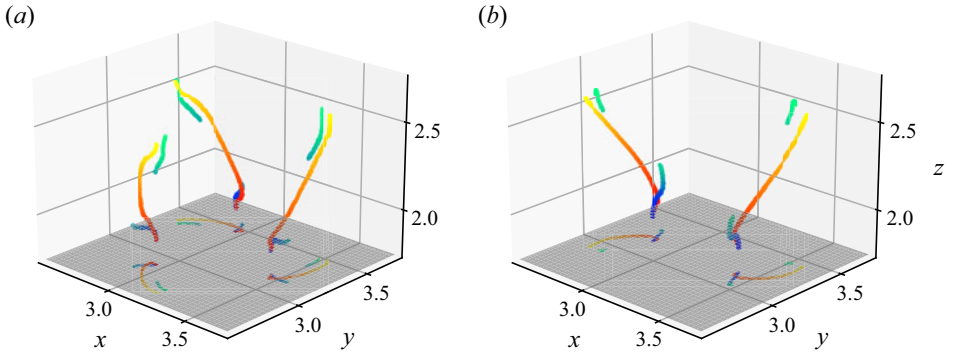


Figure 8. Three groups of trajectories of the maximum points of $|\boldsymbol{\omega}|$ (from blue to green) and $|\Delta \boldsymbol{s}|$ (from red to yellow) during $t^* \in [0, 2.2]$ for (*a*) the trefoil knot and (*b*) the Hopf link, along with their projections on the $x$–$y$ plane (shaded in grey). The two trajectories of maximum $|\boldsymbol{\omega}|$ and $|\Delta \boldsymbol{s}|$ in each group start at the same location.

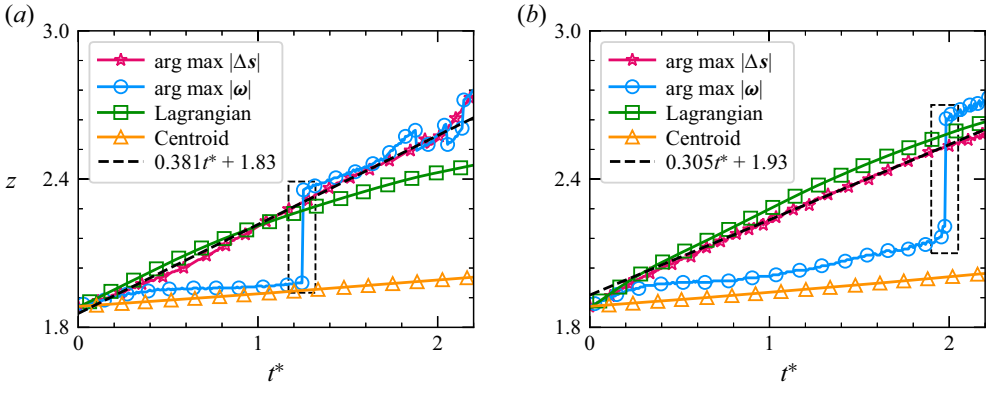


Figure 9. Evolution of the $z$-direction coordinates of the maximum points of $|\boldsymbol{\omega}|$ and $|\Delta \boldsymbol{s}|$, the Lagrangian tracing particle located at the maximum point at $t^* = 0$, and the centroid position for (*a*) the trefoil knot and (*b*) the Hopf link.

locations do not collapse, implying that the present criterion is distinct from the BKM criterion.

The continuous trajectory of $\arg\max |\Delta \boldsymbol{s}|$ is more tractable than the discontinuous one of $\arg\max |\boldsymbol{\omega}|$ in figure 8. Figure 9 illustrates the $z$-coordinates of the maximum $|\boldsymbol{\omega}|$ and $|\Delta \boldsymbol{s}|$, the Lagrangian trajectory of particles that locate at the position of the maximum values at $t^* = 0$, and the evolution of the centroid positions $z_c = \int_{s_1 \geq 0} z \, \mathrm{d}V / \int_{s_1 \geq 0} \mathrm{d}V$ of the trefoil knot and Hopf link. We find that $\arg\max |\Delta \boldsymbol{s}|$ remains continuous over time and moves at a constant speed in the $z$-direction in both flows, which is close to the Lagrangian velocity of the particle at the location of $\arg\max |\Delta \boldsymbol{s}|$ (or $\arg\max |\boldsymbol{\omega}|$) at $t^* = 0$. This implies that the maximum $|\Delta \boldsymbol{s}|$ could have some Lagrangian nature.

By contrast, $\arg\max |\boldsymbol{\omega}|$ exhibits a sharp jump at $t^* = 1.26$ for the trefoil knot and $t^* = 1.98$ for the Hopf link. The speed of $\arg\max |\boldsymbol{\omega}|$ in the $z$-direction is close to that of the centroid of the vortex at early times. During the growth of $|\boldsymbol{\omega}|$, the locus of the peak vorticity exhibits a notable displacement, converging to $\arg\max |\Delta \boldsymbol{s}|$ (marked in a dashed box in figure 9).

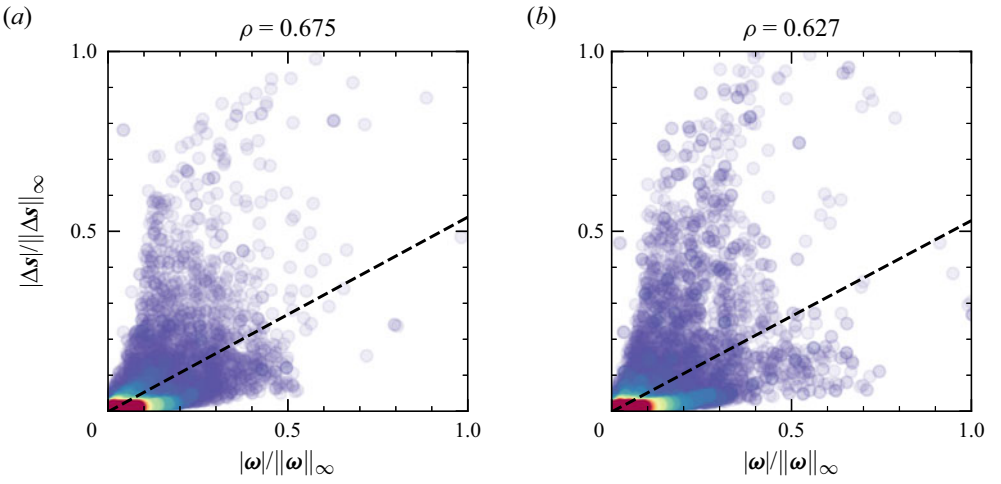


Figure 10. Scatter plots of $|\Delta \boldsymbol{s}|$ and $|\boldsymbol{\omega}|$ normalized with their maximum values for (*a*) the trefoil knot at $t^* = 1.8$, and (*b*) the Hopf link at $t^* = 2.19$, along with the correlation coefficients $\rho$ and linear fits (dashed lines) of data points. The scattered points are coloured from purple to red by the density of data points.

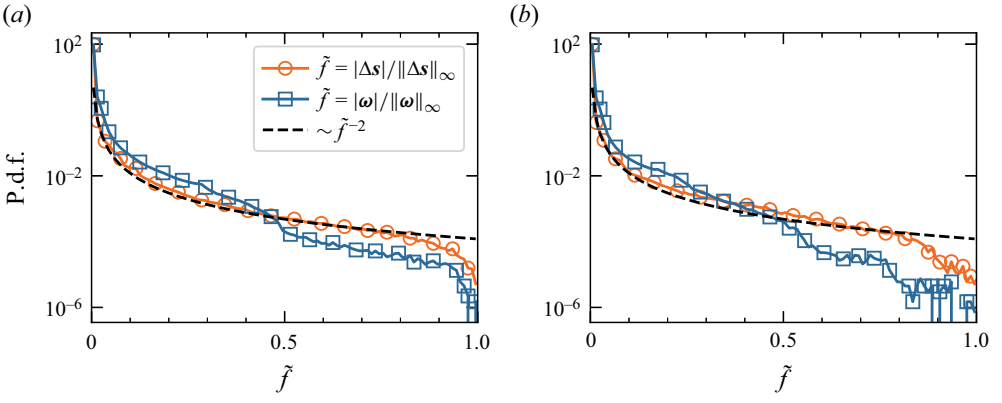


Figure 11. P.d.f.s of normalized $|\Delta \boldsymbol{s}|$ and $|\boldsymbol{\omega}|$ for (*a*) the trefoil knot at $t^* = 1.8$, and (*b*) the Hopf link at $t^* = 2.19$.

We examine the correlation and distribution of the values of $|\Delta \boldsymbol{s}|$ and $|\boldsymbol{\omega}|$, normalized by their respective maxima, for the trefoil knot at $t^* = 1.8$ and the Hopf link at $t^* = 2.19$. The scatter plots in figure 10 show a low positive correlation between $|\Delta \boldsymbol{s}|/\|\Delta \boldsymbol{s}\|_\infty$ and $|\boldsymbol{\omega}|/\|\boldsymbol{\omega}\|_\infty$, with correlation coefficients $\rho = 0.675$ for the trefoil knot, and $\rho = 0.627$ for the Hopf link. Therefore, the criterion based on $\Delta \boldsymbol{s}$ in (2.11) has a notable statistical difference from that based on $\boldsymbol{\omega}$.

The probability density functions (p.d.f.s) of the normalized values of $|\Delta \boldsymbol{s}|$ and $|\boldsymbol{\omega}|$ for the trefoil knot at $t^* = 1.8$ and the Hopf link at $t^* = 2.19$ are shown in figure 11. For both configurations, the p.d.f. profiles of $|\Delta \boldsymbol{s}|/\|\Delta \boldsymbol{s}\|_\infty$ are smoother than those of $|\boldsymbol{\omega}|/\|\boldsymbol{\omega}\|_\infty$, and they obey a Pareto distribution (Arnold 2015) with the $-2$ power law except for very large values, indicating that the extreme values at a few locations can dominate norms of $\Delta \boldsymbol{s}$ and $\boldsymbol{\omega}$.

## 5. Conclusions

We develop a new framework for describing ideal flows using the spin Euler equation (2.7). The spin Euler equation can be considered as a special Landau–Lifshitz equation with an effective magnetic field $\boldsymbol{m}$ in (2.6), implying a possible connection between the ideal flow and magnetic material.

Compared to the classical Euler equation, the spin Euler equation provides a feasible approach to study Lagrangian fluid dynamics, because the isosurfaces of a spin-vector component are vortex surfaces and material surfaces for all $t \geq 0$. In particular, we derive a non-blowup condition (2.11) for the spin Euler equation – if the solution becomes singular at some finite time, then $|\Delta \boldsymbol{s}|$ must become unbounded. Moreover, the ideal flow dynamics is formulated as a Hamiltonian simulation of a quantum mechanical system using the spin Euler equation, which can inspire the development of relevant quantum algorithms (Meng & Yang 2023).

On the other hand, the spin Euler equation does not seem to admit arbitrary velocity fields as initial conditions. The theoretical construction of a globally smooth $\boldsymbol{s}_0$ for a given velocity field remains an open problem, and it can be approximated only numerically at present.

We conduct the DNS of three ideal flows of the trefoil knot, Hopf link and MTG by solving (3.1) using the pseudo-spectral method, and compare the BKM criterion with the present one. The evolution of the vortex surface (isosurface of $s_1$) illustrates that the regions with large $|\boldsymbol{\omega}|$ are rapidly stretched into spiral sheets for the trefoil knot and Hopf link.

For the trefoil knot and Hopf link, the double-exponential growth of $\|\Delta \boldsymbol{s}\|_\infty$ is more pronounced than that of $\|\boldsymbol{\omega}\|_\infty$, and $\ln\ln\|\Delta \boldsymbol{s}\|_\infty$ grows at a rate 4–6 times slower than $\ln\ln\|\boldsymbol{\omega}\|_\infty$. The duration of the double-exponential growth stage for $\|\Delta \boldsymbol{s}\|_\infty$ exceeds that for $\|\boldsymbol{\omega}\|_\infty$ by more than five times. According to the non-blowup condition (2.11), the Euler equation can avoid the singularity formation at finite time if the growth rate of $\|\Delta \boldsymbol{s}\|_\infty$ is lower than double-exponential at late times.

The highly symmetric MTG flow can avoid finite-time singularities due to the formation of quasi-2-D vortex surfaces from theoretical analysis (Constantin *et al.* 1996). The growth rate of $\|\Delta \boldsymbol{s}\|_\infty$ is lower than double-exponential at late times, whereas the growth rate of $\|\boldsymbol{\omega}\|_\infty$ remains double-exponential. Thus the present criterion based on $\Delta \boldsymbol{s}$ appears to be more sensitive than the BKM criterion based on $\boldsymbol{\omega}$ in detecting the flows that are incapable of producing finite-time singularities.

The present non-blowup criterion based on $|\Delta \boldsymbol{s}|$ is distinct from the BKM criterion based on $|\boldsymbol{\omega}|$. By tracing the maxima of $|\Delta \boldsymbol{s}|$ and $|\boldsymbol{\omega}|$ for vortex knots and link, we find that the trajectory for $|\Delta \boldsymbol{s}|$ is continuous and consistent with the tracer particle, benefited from the Lagrangian nature of the spin Euler equation. In contrast, the trajectory for $|\boldsymbol{\omega}|$ with a large jump deviates from the Lagrangian trajectory. Furthermore, $|\Delta \boldsymbol{s}|$ and $|\boldsymbol{\omega}|$ have only a low positive correlation coefficient.

In future work, the bound estimate of $|\Delta \boldsymbol{s}|$ requires further refinement, and the duration in the simulation can be prolonged with more computational resources for examining longer growth behaviour of $\|\Delta \boldsymbol{s}\|_\infty$. Furthermore, the spin Euler equation can be recast as a nonlinear Schrödinger equation that is useful in quantum computing of fluid dynamics (Meng & Yang 2023).

**Acknowledgements.** The authors thank S. Xiong for helpful discussion. Numerical simulations were carried out on the TH-2A supercomputer in Guangzhou, China.

**Funding.** This work has been supported by the National Natural Science Foundation of China (grant nos 11925201 and 11988102), the National Key R&D Program of China (grant no. 2020YFE0204200), and the Xplorer Prize.

**Declaration of interests.** The authors report no conflict of interest.

**Author ORCIDs.**
Zhaoyuan Meng https://orcid.org/0000-0002-0933-4272;
Yue Yang https://orcid.org/0000-0001-9969-7431.

**Author contributions.** Y.Y. and Z.M. designed the research. Z.M. performed the research. Y.Y. and Z.M. discussed the results and wrote the manuscript. Both authors have given approval for the manuscript.

## Appendix A. Spherical Clebsch representation of the vorticity

Chern (2017) applied exterior calculus and quaternion formulation to derive the spherical Clebsch representation of $\boldsymbol{\omega}$ in (2.4). Here, we re-express this derivation using regular calculus. Note that equivalent forms of (2.4) appeared in Faddeev (1976) and Kuznetsov & Mikhailov (1980) without derivation.

First, we express the vorticity using Clebsch potentials by taking the curl of the velocity as

$$\boldsymbol{\omega} = \nabla \times (a\,\nabla b - b\,\nabla a + c\,\nabla d - d\,\nabla c) = 2(\nabla a \times \nabla b + \nabla c \times \nabla d). \tag{A1}$$

Then we take gradient of the three components of the spin vector as

$$\left.\begin{aligned} \nabla s_1 &= 2(a\,\nabla a + b\,\nabla b - c\,\nabla c - d\,\nabla d),\\ \nabla s_2 &= 2(b\,\nabla c + c\,\nabla b - a\,\nabla d - d\,\nabla a),\\ \nabla s_3 &= 2(a\,\nabla c + c\,\nabla a + b\,\nabla d + d\,\nabla b). \end{aligned}\right\} \tag{A2}$$

Combining $\nabla s_1 \times \nabla s_2$, $\nabla s_2 \times \nabla s_3$ and $\nabla s_3 \times \nabla s_1$, and using the normalization condition $a^2 + b^2 + c^2 + d^2 = 1$, yields

$$\begin{aligned} &s_3\,\nabla s_1 \times \nabla s_2 + s_1\,\nabla s_2 \times \nabla s_3 + s_2\,\nabla s_3 \times \nabla s_1\\ &\quad = 4(c^2 + d^2)\,\nabla a \times \nabla b + 4(ad - bc)\,\nabla a \times \nabla c - 4(ac + bd)\,\nabla a \times \nabla d\\ &\qquad + 4(ac + bd)\,\nabla b \times \nabla c + 4(ad - bc)\,\nabla b \times \nabla d + 4(a^2 + b^2)\,\nabla c \times \nabla d. \end{aligned} \tag{A3}$$

Taking the gradient of the normalization condition yields

$$a\,\nabla a + b\,\nabla b + c\,\nabla c + d\,\nabla d = \mathbf{0}. \tag{A4}$$

From (A4) and outer products of two of $\nabla a$, $\nabla b$, $\nabla c$ and $\nabla d$, we have

$$\left.\begin{aligned} b\,\nabla a \times \nabla b + c\,\nabla a \times \nabla c + d\,\nabla a \times \nabla d &= \mathbf{0},\\ a\,\nabla a \times \nabla b - c\,\nabla b \times \nabla c - d\,\nabla b \times \nabla d &= \mathbf{0},\\ a\,\nabla a \times \nabla c + b\,\nabla b \times \nabla c - d\,\nabla c \times \nabla d &= \mathbf{0},\\ a\,\nabla a \times \nabla d + b\,\nabla b \times \nabla d + c\,\nabla c \times \nabla d &= \mathbf{0}. \end{aligned}\right\} \tag{A5}$$

Substituting (A5) into (A3) yields

$$\begin{aligned} &s_3\,\nabla s_1 \times \nabla s_2 + s_1\,\nabla s_2 \times \nabla s_3 + s_2\,\nabla s_3 \times \nabla s_1\\ &\quad = 4(a^2 + b^2 + c^2 + d^2)\,\nabla a \times \nabla b + 4(a^2 + b^2 + c^2 + d^2)\,\nabla c \times \nabla d\\ &\quad = 4(\nabla a \times \nabla b + \nabla c \times \nabla d). \end{aligned} \tag{A6}$$

Finally, substituting (A6) into (A1) yields (2.4), i.e.

$$\boldsymbol{\omega} = \tfrac{1}{2}\left(s_1\,\boldsymbol{\nabla} s_2 \times \boldsymbol{\nabla} s_3 + s_2\,\boldsymbol{\nabla} s_3 \times \boldsymbol{\nabla} s_1 + s_3\,\boldsymbol{\nabla} s_1 \times \boldsymbol{\nabla} s_2\right). \tag{A7}$$

## Appendix B. Comparison of the spin Euler system and the isotropic Heisenberg spin system

It is interesting that the spin Euler equation (2.7) can be considered as the Landau–Lifshitz equation

$$\partial_t \boldsymbol{s} + \boldsymbol{s} \times \boldsymbol{H}_{eff} = \boldsymbol{0} \tag{B1}$$

without a damping term (Landau & Lifshitz 1935), which is used to analyse magnetodynamic processes in magnetic materials. Equation (B1) is also recognized as the Heisenberg model with various applications (Lakshmanan & Porsezian 1990; Porsezian & Lakshmanan 1991; Kamppeter *et al.* 2001). The Landau–Lifshitz equation plays an important role in elucidating magnetization dynamics, analogous to the role of the Navier–Stokes equation in fluid dynamics.

The mean spin of electrons, i.e. the magnetization (or spin vector) $\boldsymbol{s}$ at the macroscopic scale, determines the unit volume magnetic dipole moment in magnetic crystals. A continuous function $\boldsymbol{s}(\boldsymbol{x}, t)$ describes the macroscopic magnetization dynamics in the limit of vanishing lattice partition size, if the angle between the spin vectors of neighbouring lattice atoms in a crystal is sufficiently small (Heisenberg 1928). This resembles the continuum assumption in fluid mechanics, but unlike isotropic fluids, most crystal structures are anisotropic.

In (B1), $\boldsymbol{H}_{eff}$ is the effective magnetic field, corresponding to (minus) the $L^2$-derivative of the magnetic energy of the material with respect to $\boldsymbol{s}$. This implies a deep connection between the ideal flow and magnetic material. The spin Euler equation has $\boldsymbol{H}_{eff} = \boldsymbol{m}$, where the magnetic energy of a material is replaced by the total kinetic energy of a fluid. Therefore, the ideal flow might be physically interpreted as a specific magnetic material by (2.7).

We then discuss the similarity and difference between the spin Euler system in (2.7) and the isotropic Heisenberg spin system in (B1) with $\boldsymbol{H}_{eff} = \Delta \boldsymbol{s}$. After some algebra, we find

$$\boldsymbol{m} = \tfrac{1}{2}\,\Delta \boldsymbol{s} + \boldsymbol{m}', \tag{B2}$$

where the term

$$\begin{aligned}\boldsymbol{m}' = (&-a\,\Delta a - b\,\Delta b + c\,\Delta c + d\,\Delta d,\, a\,\Delta d + d\,\Delta a - b\,\Delta c - c\,\Delta b,\\ &-a\,\Delta c - c\,\Delta a - b\,\Delta d - d\,\Delta b)\end{aligned} \tag{B3}$$

highlights the difference between the spin Euler system and the Heisenberg spin system. Projecting $\boldsymbol{m}'$ onto $\boldsymbol{s}$ yields

$$\boldsymbol{s} \cdot \boldsymbol{m}' = -(a\,\Delta a + b\,\Delta b + c\,\Delta c + d\,\Delta d) = |\nabla \boldsymbol{\psi}|^2 \geq 0, \tag{B4}$$

i.e. the angle between $\boldsymbol{m}'$ and $\boldsymbol{s}$ is acute or normal.

As sketched in figure 12, the range of the angle $\theta \equiv \arccos((\boldsymbol{s} \cdot \boldsymbol{H}_{eff})/|\boldsymbol{H}_{eff}|)$ between $\boldsymbol{s}$ and $\boldsymbol{H}_{eff}$ depends on the spin system. The isotropic Heisenberg spin system has $\theta \in$

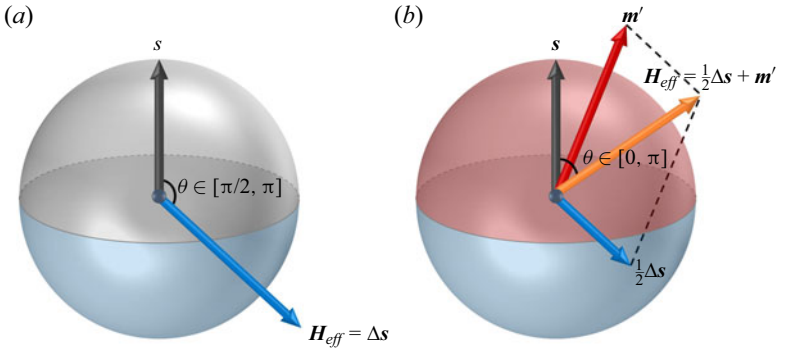


Figure 12. Schematic of orientations of the spin vector $\boldsymbol{s}$ and the effective field $\boldsymbol{H}_{eff}$ in (*a*) the isotropic Heisenberg spin system, and (*b*) the spin Euler system. The variation of $\Delta\boldsymbol{s}$ is restricted to the southern hemisphere (shaded in blue), whereas $\boldsymbol{m}'$ is restricted to the northern hemisphere (shaded in red).

$[\pi/2, \pi]$ with

$$\boldsymbol{s}\cdot\boldsymbol{H}_{eff} = \boldsymbol{s}\cdot\Delta\boldsymbol{s} = -|\nabla\boldsymbol{s}|^2 \le 0, \tag{B5}$$

whereas the spin Euler system has $\theta \in [0, \pi]$ with

$$\boldsymbol{s}\cdot\boldsymbol{H}_{eff} = \boldsymbol{s}\cdot\left(\tfrac{1}{2}\,\Delta\boldsymbol{s} + \boldsymbol{m}'\right) = |\boldsymbol{u}|^2 - \tfrac{1}{4}\,|\nabla\boldsymbol{s}|^2. \tag{B6}$$

Assuming that $\boldsymbol{H}_{eff}$ is directed to the north pole, $\boldsymbol{s}$ in the isotropic Heisenberg spin system is confined to the southern hemisphere, whereas there is no such restriction in the spin Euler system due to the additional term $\boldsymbol{m}'$. Therefore, the spin Euler system for ideal flows can have greater degrees of freedom and more complex dynamics than the isotropic Heisenberg spin system for magnetic crystals.

## Appendix C. Derivation for the non-blowup condition of the spin Euler equation

We provide the detailed derivation for the non-blowup condition (2.11) of the spin Euler equation. By taking the double inner product of $\nabla\boldsymbol{s}$ and the gradient of (2.7), and multiplying by $p\,|\nabla\boldsymbol{s}|^{2(p-1)}$, we obtain

$$\partial_t|\nabla\boldsymbol{s}|^{2p} = 2p\,|\nabla\boldsymbol{s}|^{2(p-1)}\,\nabla\boldsymbol{s} : (\nabla\boldsymbol{m}\times\boldsymbol{s}), \tag{C1}$$

where $p \ge 1$ is a constant, the double inner product is defined as $\boldsymbol{A} : \boldsymbol{B} \equiv A_{ij}B_{ij}$ with two second-order tensors $\boldsymbol{A}$ and $\boldsymbol{B}$, and the vector product of the second-order tensor $\nabla\boldsymbol{m}$ and the vector $\boldsymbol{s}$ is defined as $\nabla\boldsymbol{m}\times\boldsymbol{s} \equiv \varepsilon_{ljk}\,\partial_i m_j s_k\,\boldsymbol{e}_i\boldsymbol{e}_l$ with the basis $\{\boldsymbol{e}_1, \boldsymbol{e}_2, \boldsymbol{e}_3\}$. Using the identity $\boldsymbol{s}\cdot\Delta\boldsymbol{s} = -|\nabla\boldsymbol{s}|^2$ for the unit vector $\boldsymbol{s}$, we have

$$|\nabla\boldsymbol{s}|^2 \le |\Delta\boldsymbol{s}|. \tag{C2}$$

Integrating (C1) over a periodic domain $\mathcal{D}$ or a domain bounded by solid wall boundaries, and using (C2), yields

$$\begin{aligned}\left|\partial_t \int_{\mathcal{D}} |\nabla \boldsymbol{s}|^{2p}\,\mathrm{d}V\right| &= 2p\left|\int_{\mathcal{D}} |\nabla \boldsymbol{s}|^{2(p-1)}\,\nabla \boldsymbol{s} : (\nabla \boldsymbol{m}\times \boldsymbol{s})\,\mathrm{d}V\right| \\ &\le 2p\,\|\Delta \boldsymbol{s}\|_\infty^{p-1}\left|\int_{\mathcal{D}} [\nabla\cdot(\nabla \boldsymbol{s}\cdot(\boldsymbol{m}\times \boldsymbol{s})) + \boldsymbol{m}\cdot(\nabla\cdot(\nabla \boldsymbol{s}\times \boldsymbol{s}))]\,\mathrm{d}V\right| \\ &= 2p\,\|\Delta \boldsymbol{s}\|_\infty^{p-1}\left|\oiint_{\partial\mathcal{D}} \frac{\partial \boldsymbol{s}}{\partial n}\cdot(\boldsymbol{m}\times \boldsymbol{s})\,\mathrm{d}S\right. \\ &\quad \left. + \int_{\mathcal{D}} [\Delta \boldsymbol{s}\cdot(\boldsymbol{s}\times \boldsymbol{m}) + \nabla \boldsymbol{s} : (\nabla \boldsymbol{s}\times \boldsymbol{m})]\,\mathrm{d}V\right| \\ &= 2p\,\|\Delta \boldsymbol{s}\|_\infty^{p-1}\left|\int_{\mathcal{D}} \boldsymbol{m}\cdot(\Delta \boldsymbol{s}\times \boldsymbol{s})\,\mathrm{d}V\right|, \end{aligned} \tag{C3}$$

where the Neumann boundary condition $\partial \boldsymbol{s}/\partial n|_{\partial\mathcal{D}} = \boldsymbol{0}$ is imposed on the solid wall boundary. Applying the Hölder inequality to (C3) yields

$$\partial_t \|\nabla \boldsymbol{s}\|_{2p}^{2p} \le 2p\,\|\boldsymbol{m}\|_1\,\|\Delta \boldsymbol{s}\|_\infty^p. \tag{C4}$$

Here, the $L^p$-norm of a function $f$ is defined as

$$\|f\|_p \equiv \begin{cases} \left(\displaystyle\int_{\mathcal{D}} |f|^p\,\mathrm{d}V\right)^{1/p}, & 1\le p<\infty, \\ \operatorname{esssup}|f|, & p=\infty. \end{cases} \tag{C5}$$

We estimate the upper bound of $\|\boldsymbol{\omega}\|_p$ in terms of $\|\nabla \boldsymbol{s}\|_{2p}$. From (2.4), using $|\boldsymbol{s}| = 1$ and basic inequalities, we obtain

$$\begin{aligned}|\boldsymbol{\omega}| &\le \tfrac{1}{2}(|\nabla s_1|\,|\nabla s_2| + |\nabla s_2|\,|\nabla s_3| + |\nabla s_3|\,|\nabla s_1|) \\ &\le \tfrac{1}{2}\left[\tfrac{1}{2}(|\nabla s_1|^2 + |\nabla s_2|^2) + \tfrac{1}{2}(|\nabla s_2|^2 + |\nabla s_3|^2) + \tfrac{1}{2}(|\nabla s_3|^2 + |\nabla s_1|^2)\right] \\ &= \tfrac{1}{2}|\nabla \boldsymbol{s}|^2, \end{aligned} \tag{C6}$$

so that

$$\|\boldsymbol{\omega}\|_p \le \tfrac{1}{2}\,\|\nabla \boldsymbol{s}\|_{2p}^2. \tag{C7}$$

Then we estimate the upper bound of $\|\boldsymbol{m}\|_1$ in terms of $\|\nabla \boldsymbol{s}\|_2$ and $\|\Delta \boldsymbol{s}\|_\infty$. Substituting (C6) into (2.6), we have

$$\begin{aligned}|\boldsymbol{m}|^2 = {} & |\nabla a|^4 + |\nabla b|^4 + |\nabla c|^4 + |\nabla d|^4 + 2\,|\nabla a|^2\,|\nabla b|^2 + 2\,|\nabla c|^2\,|\nabla d|^2 \\ & - 2\,|\nabla a|^2\,|\nabla c|^2 - 2\,|\nabla a|^2\,|\nabla d|^2 - 2\,|\nabla b|^2\,|\nabla c|^2 - 2\,|\nabla b|^2\,|\nabla d|^2 \\ & + 4[(\nabla b\cdot\nabla c)^2 + (\nabla a\cdot\nabla d)^2 - 2(\nabla b\cdot\nabla c)(\nabla a\cdot\nabla d)]\end{aligned}$$

$$
\begin{aligned}
&+4[(\nabla a\cdot\nabla c)^2+(\nabla b\cdot\nabla d)^2+2(\nabla a\cdot\nabla c)(\nabla b\cdot\nabla d)]\\
&\le(|\nabla a|^2+|\nabla b|^2+|\nabla c|^2+|\nabla d|^2)^2\\
&\quad+8[(\nabla a\cdot\nabla c)(\nabla b\cdot\nabla d)-(\nabla a\cdot\nabla d)(\nabla b\cdot\nabla c)]\\
&=|\nabla\boldsymbol{\psi}|^4+8(\nabla a\times\nabla b)\cdot(\nabla c\times\nabla d)\\
&=\left(\frac{1}{4}|\nabla\boldsymbol{s}|^2+|\boldsymbol{u}|^2\right)^2+4\left(\frac{|\boldsymbol{\omega}|^2}{4}-|\nabla a\times\nabla b|^2-|\nabla c\times\nabla d|^2\right)\\
&\le\frac{1}{8}|\nabla\boldsymbol{s}|^4+2|\boldsymbol{u}|^4+|\boldsymbol{\omega}|^2\\
&\le\frac{3}{8}|\nabla\boldsymbol{s}|^4+2|\boldsymbol{u}|^4,
\end{aligned}
\tag{C8}
$$

so that

$$
\begin{aligned}
|\boldsymbol{m}|&\le\left(\tfrac{3}{8}|\nabla\boldsymbol{s}|^4+2|\boldsymbol{u}|^4\right)^{1/2}\\
&=\left[\left(\tfrac{\sqrt{6}}{4}|\nabla\boldsymbol{s}|^2+\sqrt{2}|\boldsymbol{u}|^2\right)^2-\sqrt{3}|\nabla\boldsymbol{s}|^2|\boldsymbol{u}|^2\right]^{1/2}\\
&\le\tfrac{\sqrt{6}}{4}|\nabla\boldsymbol{s}|^2+\sqrt{2}|\boldsymbol{u}|^2.
\end{aligned}
\tag{C9}
$$

Integrating (C9) over the domain $\mathcal{D}$ yields

$$
\|\boldsymbol{m}\|_1\le\tfrac{\sqrt{6}}{4}\|\nabla\boldsymbol{s}\|_2^2+\sqrt{2}\|\boldsymbol{u}\|_2^2. \tag{C10}
$$

By virtue of the Sobolev–Poincaré inequality (Moffatt & Tsinober 1992),

$$
\|\boldsymbol{u}\|_2^2\le C_\omega\|\boldsymbol{\omega}\|_2^2 \tag{C11}
$$

holds, with a positive constant $C_\omega$ independent of $\boldsymbol{u}$. Combining (C2), (C7), (C10) and (C11), we derive

$$
\begin{aligned}
\|\boldsymbol{m}\|_1&\le\tfrac{\sqrt{6}}{4}\|\nabla\boldsymbol{s}\|_2^2+\sqrt{2}C_\omega\|\boldsymbol{\omega}\|_2^2\\
&\le\tfrac{\sqrt{6}}{4}\|\nabla\boldsymbol{s}\|_2^2+\tfrac{\sqrt{2}}{4}C_\omega\|\nabla\boldsymbol{s}\|_4^4\\
&\le\tfrac{\sqrt{6}}{4}\|\nabla\boldsymbol{s}\|_2^2+\tfrac{\sqrt{2}}{4}C_\omega\|\nabla\boldsymbol{s}\|_2^2\|\Delta\boldsymbol{s}\|_\infty\\
&=\tfrac{1}{4}\|\nabla\boldsymbol{s}\|_2^2\left(\sqrt{6}+\sqrt{2}C_\omega\|\Delta\boldsymbol{s}\|_\infty\right).
\end{aligned}
\tag{C12}
$$

Finally, substituting (C12) into (C4) and applying the Hölder inequality, we have

$$
\frac{1}{\|\nabla\boldsymbol{s}\|_{2p}^{2p}}\partial_t\|\nabla\boldsymbol{s}\|_{2p}^{2p}\le\frac{p}{2}\mu^{(p-1)/p}(\mathcal{D})\left(\sqrt{6}+\sqrt{2}C_\omega\|\Delta\boldsymbol{s}\|_\infty\right)\|\Delta\boldsymbol{s}\|_\infty^p, \tag{C13}
$$

where $\mu(\mathcal{D})$ is the finite measure of domain $\mathcal{D}$. Integrating (C13) over time yields

$$
\|\nabla\boldsymbol{s}(\cdot,t)\|_2^2\le C_s\exp\left(\tfrac{1}{2}\int_0^t\left(\sqrt{6}+\sqrt{2}C_\omega\|\Delta\boldsymbol{s}(\cdot,\tau)\|_\infty\right)\|\Delta\boldsymbol{s}(\cdot,\tau)\|_\infty\,\mathrm{d}\tau\right) \tag{C14}
$$

for $p = 1$, with a constant $C_s = \exp(\|\nabla \boldsymbol{s}(\cdot, 0)\|_2^2)$, and

$$\|\nabla \boldsymbol{s}(\cdot, t)\|_{2p}^{2(p-1)} \leq \frac{p-1}{2}\,\mu^{(p-1)/p}(\mathcal{D}) \int_0^t \left(\sqrt{6}+\sqrt{2}C_\omega \|\Delta \boldsymbol{s}(\cdot, \tau)\|_\infty\right) \|\Delta \boldsymbol{s}(\cdot, \tau)\|_\infty^p \,\mathrm{d}\tau \tag{C15}$$

for $p > 1$.

As the Hölder inequality leads to

$$\int_0^t \|\Delta \boldsymbol{s}(\cdot, \tau)\|_\infty^p \,\mathrm{d}\tau \leq t^{1/(p+1)} \left(\int_0^t \|\Delta \boldsymbol{s}(\cdot, \tau)\|_\infty^{p+1} \,\mathrm{d}\tau\right)^{p/(p+1)}, \tag{C16}$$

we have

$$\begin{aligned}
&\int_0^t \left(\sqrt{6} + \sqrt{2}C_\omega \|\Delta \boldsymbol{s}(\cdot, \tau)\|_\infty\right) \|\Delta \boldsymbol{s}(\cdot, \tau)\|_\infty^p \,\mathrm{d}\tau \\
&\quad \leq \sqrt{6} t^{1/(p+1)} \left(\int_0^t \|\Delta \boldsymbol{s}(\cdot, \tau)\|_\infty^{p+1} \,\mathrm{d}\tau\right)^{p/(p+1)} + \sqrt{2}C_\omega \int_0^t \|\Delta \boldsymbol{s}(\cdot, \tau)\|_\infty^{p+1} \,\mathrm{d}\tau \\
&\quad \leq C_p(t) \int_0^t \|\Delta \boldsymbol{s}(\cdot, \tau)\|_\infty^{p+1} \,\mathrm{d}\tau, \quad \forall p \geq 1,
\end{aligned} \tag{C17}$$

where $C_p(t) = \sqrt{6} t^{1/(p+1)} + \sqrt{2}C_\omega$ is a finite coefficient when $t < \infty$. Using (C7), (C14) and (C17), the $L^1$-norm of the vorticity can be estimated by

$$\|\boldsymbol{\omega}\|_1 \leq \frac{C_s}{2} \exp\left(\frac{C_1(t)}{2} \int_0^t \|\Delta \boldsymbol{s}(\cdot, \tau)\|_\infty^2 \,\mathrm{d}\tau\right). \tag{C18}$$

Moreover, using (C7), (C15) and (C17), the $L^p$-norm ($p > 1$) of the vorticity can be estimated by

$$\|\boldsymbol{\omega}\|_p \leq \frac{1}{2} \left(\frac{p-1}{2}\,\mu^{(p-1)/p}(\mathcal{D})\, C_p(t) \int_0^t \|\Delta \boldsymbol{s}(\cdot, \tau)\|_\infty^{p+1} \,\mathrm{d}\tau\right)^{1/(p-1)}. \tag{C19}$$

From (C18) and (C19), we obtain a sufficient condition for bounded $\|\boldsymbol{\omega}\|_p$ as

$$\int_0^t \|\Delta \boldsymbol{s}(\cdot, \tau)\|_\infty^{p+1} \,\mathrm{d}\tau < \infty, \quad \forall p \geq 1, \tag{C20}$$

i.e. (2.11). Note that it is straightforward to deduce the special case of (C20) with $p = 2$ from (C6) using the BKM theorem (Beale *et al.* 1984).

## Appendix D. Upper bound estimation for $\|\Delta \boldsymbol{s}\|$

We show an attempt to estimate the upper bound of $|\Delta \boldsymbol{s}|$, which is an important ingredient in the non-blowup criterion in (2.11). Taking the inner product of $\Delta \boldsymbol{s}$ and the Laplacian of

(2.7) yields the evolution equation for $|\Delta \boldsymbol{s}|$:

$$\partial_t |\Delta \boldsymbol{s}|^2 + 2\,\Delta \boldsymbol{s} \cdot \Delta(\boldsymbol{s} \times \boldsymbol{m}) = 0. \tag{D1}$$

Integrating (D1) over $\mathcal{D}$ yields

$$\begin{aligned}
\partial_t \|\Delta \boldsymbol{s}\|_2^2 &= -2 \int_{\mathcal{D}} \varepsilon_{jrs}\, \Delta s_j \frac{\partial}{\partial x_k} \left( \frac{\partial s_r}{\partial x_k} m_s + s_r \frac{\partial m_s}{\partial x_k} \right) \mathrm{d}V \\
&= -2 \oiint_{\partial \mathcal{D}} \varepsilon_{jrs} n_k\, \Delta s_j \left( \frac{\partial s_r}{\partial x_k} m_s + s_r \frac{\partial m_s}{\partial x_k} \right) \mathrm{d}S \\
&\quad + 2 \int_{\mathcal{D}} \varepsilon_{jrs} \frac{\partial \Delta s_j}{\partial x_k} \left( \frac{\partial s_r}{\partial x_k} m_s + s_r \frac{\partial m_s}{\partial x_k} \right) \mathrm{d}V \\
&= 2 \oiint_{\partial \mathcal{D}} \varepsilon_{jrs} n_k \frac{\partial \Delta s_j}{\partial x_k} s_r m_s \,\mathrm{d}S - 2 \int_{\mathcal{D}} \varepsilon_{jrs}\, \Delta^2 s_j s_r\, m_s \,\mathrm{d}V \\
&= -2 \int_{\mathcal{D}} \Delta^2 \boldsymbol{s} \cdot (\boldsymbol{s} \times \boldsymbol{m}) \,\mathrm{d}V.
\end{aligned} \tag{D2}$$

Applying the Hölder inequality to (D2), we obtain

$$\begin{aligned}
\partial_t \|\Delta \boldsymbol{s}\|_2^2 &\le \tfrac{1}{2} \left( \sqrt{6}\, \|\Delta \boldsymbol{s}\|_1 + \sqrt{2} C_\omega\, \|\Delta \boldsymbol{s}\|_2^2 \right) \|\Delta^2 \boldsymbol{s}\|_\infty \\
&\le \tfrac{1}{2} \left( \sqrt{6} \mu^{1/2}(\mathcal{D})\, \|\Delta \boldsymbol{s}\|_2 + \sqrt{2} C_\omega\, \|\Delta \boldsymbol{s}\|_2^2 \right) \|\Delta^2 \boldsymbol{s}\|_\infty,
\end{aligned} \tag{D3}$$

which yields

$$\partial_t \|\Delta \boldsymbol{s}\|_2 \le \tfrac{1}{4} \left( \sqrt{6} \mu^{1/2}(\mathcal{D}) + \sqrt{2} C_\omega \|\Delta \boldsymbol{s}\|_2 \right) \|\Delta^2 \boldsymbol{s}\|_\infty. \tag{D4}$$

Integrating (D4) over time yields

$$\|\Delta \boldsymbol{s}\|_2 \le C_{s1} \exp\left( \frac{\sqrt{2} C_\omega}{4} \int_0^t \|\Delta^2 \boldsymbol{s}(\cdot, \tau)\|_\infty \,\mathrm{d}\tau \right) + C_{s2}, \tag{D5}$$

with constants

$$C_{s1} = \frac{1}{\sqrt{2} C_\omega} \left( \sqrt{6} \mu^{1/2}(\mathcal{D}) + \sqrt{2} C_\omega\, \|\Delta \boldsymbol{s}(\cdot, 0)\|_2 \right), \quad C_{s2} = -\frac{\sqrt{3} \mu^{1/2}(\mathcal{D})}{C_\omega}. \tag{D6a,b}$$

The inequality (D5) implies a closure problem in the bound estimation – the growth of the $L^2$-norm of $\Delta \boldsymbol{s}$ depends on its higher-order derivatives. In addition, using the identity

$$\Delta \boldsymbol{s} \cdot \Delta(\boldsymbol{s} \times \boldsymbol{m}) = \Delta \boldsymbol{s} \cdot (\boldsymbol{s} \times \Delta \boldsymbol{m}) + 2\, \nabla \boldsymbol{s} : (\nabla \boldsymbol{m} \times \Delta \boldsymbol{s}), \tag{D7}$$

we estimate the growth rate of the $L^\infty$-norm of $\Delta \boldsymbol{s}$ as

$$\partial_t \|\Delta \boldsymbol{s}\|_\infty \le \|\Delta \boldsymbol{m}\|_\infty + \|\nabla \boldsymbol{m}\|_\infty\, \|\Delta \boldsymbol{s}\|_\infty^{1/2}. \tag{D8}$$

However, it appears to be challenging to estimate $\|\Delta \boldsymbol{m}\|_\infty$ and $\|\nabla \boldsymbol{m}\|_\infty$ in terms of $\|\Delta \boldsymbol{s}\|_\infty$. Thus the estimations of (D5) and (D8) need to be improved in future work.

## References


Agafontsev, D.S., Kuznetsov, E.A. & Mailybaev, A.A. 2015 Development of high vorticity structures in incompressible 3D Euler equations. *Phys. Fluids* **27**, 085102.

Agafontsev, D.S., Kuznetsov, E.A. & Mailybaev, A.A. 2017 Asymptotic solution for high-vorticity regions in incompressible three-dimensional Euler equations. *J. Fluid Mech.* **813**, R1.

Aref, H. & Zawadzki, I. 1991 Linking of vortex rings. *Nature* **354**, 50–53.

Arnold, B.C. 2015 *Pareto Distribution* . Wiley Online Library: https://doi.org/10.1002/9781118445112.stat01100.pub2.

Ayala, D. & Protas, B. 2017 Extreme vortex states and the growth of enstrophy in three-dimensional incompressible flows. *J. Fluid Mech.* **818**, 772–806.

Beale, J.T., Kato, T. & Majda, A. 1984 Remarks on the breakdown of smooth solutions for the 3-D Euler equations. *Commun. Math. Phys.* **94**, 61–66.

Boratav, O.N. & Pelz, R.B. 1994 Direct numerical simulation of transition to turbulence from a high-symmetry initial condition. *Phys. Fluids* **6**, 2757–2784.

Brachet, M.E., Meiron, D.I., Orszag, S.A., Nickel, B.G., Morf, R.H. & Frisch, U. 1983 Small-scale structure of the Taylor–Green vortex. *J. Fluid Mech.* **130**, 411–452.

Brachet, M.E., Meneguzzi, M., Vincent, A., Politano, H. & Sulem, P.L. 1992 Numerical evidence of smooth self-similar dynamics and possibility of subsequent collapse for three-dimensional ideal flows. *Phys. Fluids* A **4**, 2845–2854.

Bustamante, M.D. & Brachet, M. 2012 Interplay between the Beale–Kato–Majda theorem and the analyticity-strip method to investigate numerically the incompressible Euler singularity problem. *Phys. Rev.* E **86**, 066302.

Bustamante, M.D. & Kerr, R.M. 2008 3D Euler about a 2D symmetry plane. *Physica* D **237**, 1912–1920.

Campolina, C.S. & Mailybaev, A.A. 2018 Chaotic blowup in the 3D incompressible Euler equations on a logarithmic lattice. *Phys. Rev. Lett.* **121**, 064501.

Chae, D. 2008 Incompressible Euler equations: the blow-up problem and related results. In *Handbook of Differential Equations: Evolutionary Equations* (ed. C.M. Dafermos & M. Pokorny), vol. 4, pp. 1–55. Elsevier.

Chern, A. 2017 Fluid dynamics with incompressible Schrödinger flow. PhD thesis, California Institute of Technology, Pasadena, CA.

Chern, A., Knöppel, F., Pinkall, U. & Schröder, P. 2017 Inside fluids: Clebsch maps for visualization and processing. *ACM Trans. Graph.* **36**, 1–11.

Chern, A., Knöppel, F., Pinkall, U., Schröder, P. & Weissmann, S. 2016 Schrödinger's smoke. *ACM Trans. Graph.* **35**, 1–13.

Chorin, A.J. 1994 Vortex phase transitions in $2\frac{1}{2}$ dimensions. *J. Stat. Phys.* **76**, 835–856.

Constantin, P. 2001*a* An Eulerian–Lagrangian approach for incompressible fluids: local theory. *J. Am. Math. Soc.* **14**, 263–278.

Constantin, P. 2001*b* An Eulerian–Lagrangian approach to the Navier–Stokes equations. *Commun. Math. Phys.* **216**, 663–686.

Constantin, P., Fefferman, C. & Majda, A.J. 1996 Geometric constraints on potentially singular solutions for the 3-D Euler equations. *Commun. Part. Diff. Equ.* **21**, 559–571.

Deng, J., Hou, T.Y. & Yu, X. 2005 A level set formulation for the 3D incompressible Euler equations. *Meth. Appl. Anal.* **12**, 427–440.

Doering, C.R. 2009 The 3D Navier–Stokes problem. *Annu. Rev. Fluid Mech.* **41**, 109–128.

Drivas, T.D. & Elgindi, T.M. 2023 Singularity formation in the incompressible Euler equation in finite and infinite time. *EMS Surv. Math. Sci.* **10** (1), 1–100.

Elgindi, T.M. 2021 Finite-time singularity formation for $C^{1,\alpha}$ solutions to the incompressible Euler equations on $\mathbb{R}^3$. *Ann. Maths* **194**, 647–727.

Faddeev, L.D. 1976 Some comments on the many-dimensional solitons. *Lett. Math. Phys.* **1**, 289–293.

Fefferman, C. 2001 Existence and smoothness of the Navier–Stokes equation. *The Millennium Prize Problems* 57, 67. Clay Mathematics Institute.

Gibbon, J.D. 2008 The three-dimensional Euler equations: where do we stand? *Physica* D **237**, 1894–1904.

Gibbon, J.D. & Holm, D.D. 2007 Lagrangian particle paths and ortho-normal quaternion frames. *Nonlinearity* **20**, 1745–1759.

Grafke, T., Homann, H., Dreher, J. & Grauer, R. 2008 Numerical simulations of possible finite time singularities in the incompressible Euler equations: comparison of numerical methods. *Physica* D **237**, 1932–1936.

Grauer, R., Marliani, C. & Germaschewski, K. 1998 Adaptive mesh refinement for singular solutions of the incompressible Euler equations. *Phys. Rev. Lett.* **80**, 4177–4180.

HEISENBERG, W. 1928 Zur Theorie des Ferromagnetismus. *Z. Phys.* **49**, 619–636.
HOPF, H. 1931 Über die Abbildungen der Dreidimensionalen Sphäre auf die Kugelfläche. *Math. Ann.* **104**, 637–665.
HOU, T.Y. 2009 Blow-up or no blow-up? A unified computational and analytic approach to 3D incompressible Euler and Navier–Stokes equations. *Acta Numerica* **18**, 277–346.
HOU, T.Y. & LI, R. 2007 Computing nearly singular solutions using pseudo-spectral methods. *J. Comput. Phys.* **226**, 379–397.
HOU, T.Y. & LI, R. 2008 Blowup or no blowup? The interplay between theory and numerics. *Physica* D **237**, 1937–1944.
KAMPPETER, T., LEONEL, S.A., MERTENS, F.G., GOUVÊA, M.E., PIRES, A.S.T. & KOVALEV, A.S. 2001 Topological and dynamical excitations in a classical 2D easy-axis Heisenberg model. *Eur. Phys. J.* B **21**, 93–102.
KEDIA, H., FOSTER, D., DENNIS, M.R. & IRVINE, W.T.M. 2016 Weaving knotted vector fields with tunable helicity. *Phys. Rev. Lett.* **117**, 274501.
KERR, R.M. 1993 Evidence for a singularity of the three-dimensional, incompressible Euler equations. *Phys. Fluids* A **5**, 1725–1746.
KERR, R.M. 2005 Velocity and scaling of collapsing Euler vortices. *Phys. Fluids* **17**, 075103.
KERR, R.M. 2013 Bounds for Euler from vorticity moments and line divergence. *J. Fluid Mech.* **729**, R2.
KIDA, S. 1985 Three-dimensional periodic flows with high-symmetry. *J. Phys. Soc. Japan* **54**, 2132–2136.
KIVOTIDES, D. & LEONARD, A. 2021 Helicity spectra and topological dynamics of vortex links at high Reynolds numbers. *J. Fluid Mech.* **911**, A25.
KUZNETSOV, E.A. & MIKHAILOV, A.V. 1980 On the topological meaning of canonical Clebsch variables. *Phys. Lett.* A **77**, 37–38.
LAKSHMANAN, M. & PORSEZIAN, K. 1990 Planar radially symmetric Heisenberg spin system and generalized nonlinear Schrödinger equation: gauge equivalence, Bäcklund transformations and explicit solutions. *Phys. Lett.* A **146**, 329–334.
LANDAU, L. & LIFSHITZ, E. 1935 On the theory of the dispersion of magnetic permeability in ferromagnetic bodies. *Phys. Zeitsch. Sow.* **8**, 153–169.
MAJDA, A.J. & BERTOZZI, A.L. 2002 *Vorticity and Incompressible Flow*. Cambridge University Press.
MENG, Z., SHEN, W. & YANG, Y. 2023 Evolution of dissipative fluid flows with imposed helicity conservation. *J. Fluid Mech.* **954**, A36.
MENG, Z. & YANG, Y. 2023 Quantum computing of fluid dynamics using the hydrodynamic Schrödinger equation. *Phys. Rev. Res.* **5**, 033182.
MOFFATT, H.K. 1969 The degree of knottedness of tangled vortex lines. *J. Fluid Mech.* **35**, 117–129.
MOFFATT, H.K. & TSINOBER, A. 1992 Helicity in laminar and turbulent flow. *Annu. Rev. Fluid Mech.* **24**, 281–312.
MOREAU, J.J. 1961 Constantes d'un îlot tourbillonnaire en fluide parfait barotrope. *C. R. Acad. Sci. Paris* **252**, 2810–2812.
NABIZADEH, M.S., WANG, S., RAMAMOORTHI, R. & CHERN, A. 2022 Covector fluids. *ACM Trans. Graph.* **41**, 1–16.
ORLANDI, P., PIROZZOLI, S. & CARNEVALE, G.F. 2012 Vortex events in Euler and Navier–Stokes simulations with smooth initial conditions. *J. Fluid Mech.* **690**, 288–320.
PELZ, R.B. 2001 Symmetry and the hydrodynamic blow-up problem. *J. Fluid Mech.* **444**, 299–320.
PLANCHON, F. 2003 An extension of the Beale–Kato–Majda criterion for the Euler equations. *Commun. Math. Phys.* **232**, 319–326.
POINCARÉ, H. 1890 Sur le problème des trois corps et les équations de la dynamique. *Acta Mathematica* **13**, 1–270.
PORSEZIAN, K. & LAKSHMANAN, M. 1991 On the dynamics of the radially symmetric Heisenberg ferromagnetic spin system. *J. Math. Phys.* **32**, 2923–2928.
PUMIR, A. & SIGGIA, E. 1990 Collapsing solutions to the 3-D Euler equations. *Phys. Fluids* A **2**, 220–241.
RICCA, R.L., SAMUELS, D.C. & BARENGHI, C.F. 1999 Evolution of vortex knots. *J. Fluid Mech.* **391**, 29–44.
SHEN, W., YAO, J., HUSSAIN, F. & YANG, Y. 2023 Role of internal structures within a vortex in helicity dynamics. *J. Fluid Mech.* **970**, A26.
TAO, R., REN, H., TONG, Y. & XIONG, S. 2021 Construction and evolution of knotted vortex tubes in incompressible Schrödinger flow. *Phys. Fluids* **33**, 077112.
TAYLOR, G.I. & GREEN, A.E. 1937 Mechanism of the production of small eddies from large ones. *Proc. R. Soc. Lond.* A **158**, 499–521.

WEI, D. 2016 Regularity criterion to the axially symmetric Navier–Stokes equations. *J. Math. Anal. Applics.* **435**, 402–413.

XIONG, S., WANG, Z., WANG, M. & ZHU, B. 2022 A Clebsch method for free-surface vortical flow simulation. *ACM Trans. Graph.* **41**, 116.

XIONG, S. & YANG, Y. 2019 Identifying the tangle of vortex tubes in homogeneous isotropic turbulence. *J. Fluid Mech.* **874**, 952–978.

XIONG, S. & YANG, Y. 2020 Effects of twist on the evolution of knotted magnetic flux tubes. *J. Fluid Mech.* **895**, A28.

YANG, S., XIONG, S., ZHANG, Y., FENG, F., LIU, J. & ZHU, B. 2021 Clebsch gauge fluid. *ACM Trans. Graph.* **40**, 1–11.

YANG, Y. & PULLIN, D.I. 2010 On Lagrangian and vortex-surface fields for flows with Taylor–Green and Kida–Pelz initial conditions. *J. Fluid Mech.* **661**, 446–481.

YANG, Y. & PULLIN, D.I. 2011 Evolution of vortex-surface fields in viscous Taylor–Green and Kida–Pelz flows. *J. Fluid Mech.* **685**, 146–164.

YANG, Y., XIONG, S. & LU, Z. 2023 Applications of the vortex-surface field to flow visualization, modelling and simulation. *Flow* **3**, E33.

YAO, J. & HUSSAIN, F. 2022 Vortex reconnection and turbulence cascade. *Annu. Rev. Fluid Mech.* **54**, 317–347.

YAO, J., SHEN, W., YANG, Y. & HUSSAIN, F. 2022 Helicity dynamics in viscous vortex links. *J. Fluid Mech.* **944**, A41.

YAO, J., YANG, Y. & HUSSAIN, F. 2021 Dynamics of a trefoil knotted vortex. *J. Fluid Mech.* **923**, A19.

YUDOVICH, V.I. 1963 Non-stationary flows of an ideal incompressible fluid. *Z. Vychisl. Mat. i Mat. Fiz.* **3**, 1032–1066.

ZHAO, X. & SCALO, C. 2021 Helicity dynamics in reconnection events of topologically complex vortex flows. *J. Fluid Mech.* **920**, A30.

ZHAO, X., YU, Z., CHAPELIER, J. & SCALO, C. 2021 Direct numerical and large-eddy simulation of trefoil knotted vortices. *J. Fluid Mech.* **910**, A31.

ZHOU, Y. & LEI, Z. 2013 Logarithmically improved criteria for Euler and Navier–Stokes equations. *Commun. Pure Appl. Anal.* **12**, 2715–2719.